Theoretical And Computational Study of Steady Transonic Flows of Bethe-Zel'dovich-Thompson Fluids

Aleksandr V. Andreyev

Thesis submitted to the Faculty of the
Virginia Polytechnic Institute and State University
in partial fulfillment of the requirements for the degree of

Master of Science
in
Engineering Mechanics

Mark S. Cramer, Chair
Sungwhun Jung
Saad A. Ragab

August 25, 2013
Blacksburg, Virginia

Keywords: Transonic Flow, Bethe-Zel'dovich-Thompson, Small Disturbance, Successive Line Relaxation, Shock Splitting

Theoretical And Computational Study of Steady Transonic Flows of Bethe-Zel'dovich-Thompson Fluids

Aleksandr V. Andreyev

We examine steady transonic flows of Bethe-Zeldovich-Thompson (BZT) fluids over thin turbine blades or airfoils. BZT fluids are ordinary fluids having a region of negative fundamental derivative over a finite range of pressures and temperatures in the single phase regime. We derive the transonic small disturbance equation (TSDE) capable of capturing the qualitative behavior of BZT fluids. The shock jump conditions, and shock existence conditions consistent with the derived TSDE are presented. The flux function is seen to be quartic in the pressure or density perturbation rather than the quadratic (convex) flux function of the perfect gas theory. We show how this nonconvex flux function can be used to predict and explain the complex flows possible in transonic BZT fluids. Numerical solutions using a successive line relaxation (SLR) scheme are presented. New results of interest include shock-splitting, collisions between expansion and compression shocks, the prediction and observation of two compressive bow shocks in supersonic flows, and the observation of as many as three normal stern shocks following an oblique trailing edge shock.

Contents

1 Introduction **1**

2 Formulation **6**

3 Full Potential Equation **8**

4 Universal Transonic Small Disturbance Equation **11**

5 Non-classical Transonic Small Disturbance Equation **13**

6 Shocks and Shock Existence **18**

7 Numerical Scheme **22**

8 Validation **25**

9 Results **31**
9.0.1 Case 1: Subsonic Free Stream Flow With $K_2 > 0$ and $K_3 > 0$ 31
9.0.2 Case 2: Subsonic Free Stream Flow With $K_2 > 0$ and $K_3 < 0$ 46
9.0.3 Case 3: Supersonic Free Stream Flow With $K_2 < 0$ and $K_3 > 0$ . . . 61

10 Summary **66**

List of Figures

1.1 Variation of the fundamental derivative with density 4

3.1 Wing shape of a NACA 00XX wing with free stream conditions of U, ρ_∞, and T_∞. 9

5.1 Typical shape of the F curve. The value of $K_1 = 1$, $K_2 = 1$, and $K_3 = 0.4$. 17

6.1 Example Rayleigh lines for admissible shock jumps directions. The lowest most Rayleigh line represents an expansion shock. The value of $K_1 = 1$, $K_2 = 0.9$, and $K_3 = 0.34$. 20

6.2 Example of Shock-Splitting. If the proposed discontinuity is $1 \to 4$, the shock splits into the oblique shock from $1 \to 2$, an isotropic compression, and the oblique shock from $3 \to 4$. The value of $K_1 = 1$, $K_2 = 0.9$, and $K_3 = 0.34$. . 21

7.1 Mesh with uniformity in $\hat{y}$ ending at $\hat{y} = 2$ in the vertical direction and with uniformity ending at $\bar{x} = -2$ and $\bar{x} = \frac{1}{2}$ in the horizontal direction. 24

8.1 Comparison of the numerical solution with increasing amount of points on a circular arc wing compared to exact analytical solution at $\hat{y} = 0$. 26

8.2 Comparison of the numerical solution with increasing amount of points on a circular arc wing compared to exact analytical solution at $\bar{x} = 0$. 27

8.3 Grid convergence test of the numerical solution on the NACA 00XX wing ($\hat{y} = 0$) of the classic transonic small disturbance equations with increasing amount of grid points. 28

8.4 Numerical solution of the non-classical transonic small disturbance equations on the NACA 00XX wing ($\hat{y} = 0$) with increasing boundary distance, with a subsonic free stream, and with $M_\infty \approx 1$, $K_1 = 0.05, K_2 = 1.35, K_3 = 0.69$. . . 30

8.5 Numerical solution of the non-classical transonic small disturbance equations on the NACA 00XX wing ($\hat{y} = 0$) with increasing boundary distance, with a supersonic free stream, and with $M_\infty \approx 1$, $K_1 = -1, K_2 = -0.9, K_3 = 0.34$. . 30

9.1 F curves for the first case with varying K_1 and $K_2 = 1.35, K_3 = 0.69$. 32

9.2 Density distribution of a subsonic free stream flow with $\beta = 1$ and $K_1 = 1, K_2 = 1.35$, and $K_3 = 0.69$. 32

9.3 Contour plot of the density distribution of a subsonic free stream flow with $\beta = 1$ and $K_1 = 1, K_2 = 1.35$, and $K_3 = 0.69$. Contour steps of $\Delta\hat{\rho} = 0.1$ . . 33
9.4 Mach number distribution of a subsonic free stream flow with $\beta = 1$ and $K_1 = 1, K_2 = 1.35$, and $K_3 = 0.69$ 33
9.5 Density distribution of a subsonic free stream flow with $\beta = 1.3$ and $K_1 = 1, K_2 = 1.35$, and $K_3 = 0.69$ 34
9.6 Contour plot of the density distribution of a subsonic free stream flow with $\beta = 1.3$ and $K_1 = 1, K_2 = 1.35$, and $K_3 = 0.69$. Contour steps of $\Delta\hat{\rho} = 0.1$. 35
9.7 Mach number distribution of a subsonic free stream flow with $\beta = 1.3$ and $K_1 = 1, K_2 = 1.35$, and $K_3 = 0.69$ 35
9.8 Rayleigh lines describing the strength and the type of shock waves present in the flow for the case with $\beta = 0.5$ and $K_1 = 0.6, K_2 = 1.35$, and $K_3 = 0.69$. . 37
9.9 Density distribution of a subsonic free stream flow with $\beta = 0.5$ and $K_1 = 0.6, K_2 = 1.35$, and $K_3 = 0.69$. 37
9.10 Contour plot of the density distribution of a subsonic free stream flow with $\beta = 0.5$ and $K_1 = 0.6, K_2 = 1.35$, and $K_3 = 0.69$. Contour steps of $\Delta\hat{\rho} = 0.1$ 38
9.11 Rayleigh lines describing the strength and the type of shock waves present in the flow for the case with $\beta = 0.7$ and$K_1 = 0.6, K_2 = 1.35$, and $K_3 = 0.69$. . 39
9.12 Density distribution of a subsonic free stream flow with $\beta = 0.7$ and $K_1 = 0.6, K_2 = 1.35$, and $K_3 = 0.69$. 39
9.13 Contour plot of the density distribution of a subsonic free stream flow with $\beta = 0.7$ and $K_1 = 0.6, K_2 = 1.35$, and $K_3 = 0.69$. Contour steps of $\Delta\hat{\rho} = 0.1$ 40
9.14 Rayleigh lines describing the strength and the type of shock waves present in the flow for the case with $\beta = 1.1$ and $K_1 = 0.6, K_2 = 1.35$, and $K_3 = 0.69$. The split shock is indicated in red. 41
9.15 Density distribution of a subsonic free stream flow with $\beta = 1.1$ and $K_1 = 0.6, K_2 = 1.35$, and $K_3 = 0.69$. 41
9.16 Contour plot of the density distribution of a subsonic free stream flow with $\beta = 1.1$ and $K_1 = 0.6, K_2 = 1.35$, and $K_3 = 0.69$. Contour steps of $\Delta\hat{\rho} = 0.1$ 42
9.17 Rayleigh lines describing the strength and the type of shock waves present in the flow for the case with $\beta = 2$ and $K_1 = 0.6, K_2 = 1.35$, and $K_3 = 0.69$. The shock collision is indicated in red and the resultant shock is indicated in green. 43
9.18 Density distribution of a subsonic free stream flow with $\beta = 2$ and $K_1 = 0.6, K_2 = 1.35$, and $K_3 = 0.69$. 43
9.19 Contour plot of the density distribution of a subsonic free stream flow with $\beta = 2$ and $K_1 = 0.6, K_2 = 1.35$, and $K_3 = 0.69$. Contour steps of $\Delta\hat{\rho} = 0.1$. 44
9.20 Rayleigh lines describing the strength and the type of shock waves present in the flow for the case with $\beta = 1$ and $K_1 = 0.05, K_2 = 1.35$, and $K_3 = 0.69$. . 45
9.21 Density distribution of a subsonic free stream flow with $\beta = 1$ and $K_1 = 0.05, K_2 = 1.35$, and $K_3 = 0.69$. 45

9.22 Contour plot of the density distribution of a subsonic free stream flow with $\beta = 1$ and $K_1 = 0.05, K_2 = 1.35$, and $K_3 = 0.69$. Contour steps of $\Delta\hat{\rho} = 0.2$. 46
9.23 F curves for the second case with varying K_1 and $K_2 = 0.1, K_3 = -4$. 47
9.24 Mach number distribution of a subsonic free stream flow with $\beta = 0.7$ and $K_1 = 1, K_2 = 0.1$ and $K_3 = -4$. 48
9.25 Density distribution of a subsonic free stream flow with $\beta = 0.7$ and $K_1 = 1, K_2 = 0.1$ and $K_3 = -4$. 48
9.26 Contour plot of the density distribution of a subsonic free stream flow with $\beta = 0.7$ and $K_1 = 1, K_2 = 0.1$ and $K_3 = -4$. Contour steps of $\Delta\hat{\rho} = 0.1$ . . . 49
9.27 Rayleigh lines describing the strength and the type of shock waves present in the flow for the case with $\beta = 0.3$ and $K_1 = 0.6, K_2 = 0.1$, and $K_3 = -4$. . . 51
9.28 Density distribution of a subsonic free stream flow with $\beta = 0.3$ and $K_1 = 0.6, K_2 = 0.1$ and $K_3 = -4$. 51
9.29 Contour plot of the density distribution of a subsonic free stream flow with $\beta = 0.3$ and $K_1 = 0.6, K_2 = 0.1$, and $K_3 = -4$. Contour steps of $\Delta\hat{\rho} = 0.1$ . . 52
9.30 Rayleigh lines describing the strength and the type of shock waves present in the flow for the case with $\beta = 0.5$ and $K_1 = 0.6, K_2 = 0.1$, and $K_3 = -4$. . . 53
9.31 Density distribution of a subsonic free stream flow with $\beta = 0.5$ and $K_1 = 0.6, K_2 = 0.1$ and $K_3 = -4$. 53
9.32 Contour plot of the density distribution of a subsonic free stream flow with $\beta = 0.5$ and $K_1 = 0.6, K_2 = 0.1$, and $K_3 = -4$. Contour steps of $\Delta\hat{\rho} = 0.1$ . . 54
9.33 Density distribution of a subsonic free stream flow with $\beta = 0.7$ and $K_1 = 0.6, K_2 = 0.1$ and $K_3 = -4$. 55
9.34 Contour plot of the density distribution of a subsonic free stream flow with $\beta = 0.7$ and $K_1 = 0.6, K_2 = 0.1$, and $K_3 = -4$. Contour steps of $\Delta\hat{\rho} = 0.1$ . . 55
9.35 Rayleigh lines describing the strength and the type of shock waves present in the flow for the case with $\beta = 0.9$ and $K_1 = 0.6, K_2 = 0.1$, and $K_3 = -4$. . . 56
9.36 Density distribution of a subsonic free stream flow with $\beta = 0.9$ and $K_1 = 0.6, K_2 = 0.1$ and $K_3 = -4$. 57
9.37 Contour plot of the density distribution of a subsonic free stream flow with $\beta = 0.9$ and $K_1 = 0.6, K_2 = 0.1$, and $K_3 = -4$. Contour steps of $\Delta\hat{\rho} = 0.1$ . . 57
9.38 Rayleigh lines describing the strength and the type of shock waves present in the flow for the case with $\beta = 1.2$ and $K_1 = 0.6, K_2 = 0.1$, and $K_3 = -4$. . . 58
9.39 Density distribution of a subsonic free stream flow with $\beta = 1.2$ and $K_1 = 0.6, K_2 = 0.1$ and $K_3 = -4$. 59
9.40 Mach number distribution of a subsonic free stream flow with $\beta = 1.2$ and $K_1 = 1, K_2 = 0.1$ and $K_3 = -4$. 59
9.41 Contour plot of the density distribution of a subsonic free stream flow with $\beta = 1.2$ and $K_1 = 0.6, K_2 = 0.1$, and $K_3 = -4$. Contour steps of $\Delta\hat{\rho} = 0.1$ . . 60
9.42 Two shocks close together with $\beta = 1.2$ and $K_1 = 0.6, K_2 = 0.1$, and $K_3 = -4$. Contour steps of $\Delta\hat{\rho} = 0.1$ 60
9.43 F curves for the third case with varying K_1 and $K_2 = -0.9, K_3 = 0.34$. . . . 61

9.44 Rayleigh lines describing the strength and the type of shock waves present in the flow for the case with $\beta = 1$ and $K_1 = -1, K_2 = -0.9$, and $K_3 = 0.34$. . . 62
9.45 Density distribution of a supersonic free stream flow with $\beta = 1$ and $K_1 = -1, K_2 = -0.9$, and $K_3 = 0.34$. 62
9.46 Contour plot of the density distribution of a supersonic free stream flow with $\beta = 1$ and $K_1 = -1, K_2 = -0.9$, and $K_3 = 0.34$. Contour steps of $\Delta\hat{\rho} = 0.1$. 63
9.47 Rayleigh lines describing the strength and the type of shock waves present in the flow for the case with $\beta = 1$ and $K_1 = -1.3, K_2 = -0.9$, and $K_3 = 0.34$. . 64
9.48 Density distribution of a supersonic free stream flow with $\beta = 1$ and $K_1 = -1.3, K_2 = -0.9$, and $K_3 = 0.34$. 64
9.49 Contour plot of the density distribution of a supersonic free stream flow with $\beta = 1$ and $K_1 = -1.3, K_2 = -0.9$, and $K_3 = 0.34$.. Contour steps of $\Delta\hat{\rho} = 0.1$ 65
9.50 Contour plot of the density distribution at the collision of the leading bow shock with the expansion shock of a supersonic free stream flow with $\beta = 1$ and $K_1 = -1.3, K_2 = -0.9$, and $K_3 = 0.34$. Contour steps of $\Delta\hat{\rho} = 0.1$ . . . 65

List of Tables

8.1 $K_1 = 2.9$ Compared to Calculated K_1 for Different Resolutions 29

Chapter 1

Introduction

In traditional aerodynamics, transonic flow is defined as the transition region between the pure subsonic and pure supersonic regimes. This range of flow speeds is of great importance to designs of high-speed commercial and military aircraft, propulsion systems, and power systems. In addition to modifying the basic lift distribution and centers of pressure, the adverse pressure gradients associated with the unavoidable compression shocks give rise to separation, large increases in drag and loss, as well as unwanted vibration and loss of effectiveness of control surfaces. In fact, the term sound barrier refers to the large increase in drag found in the transonic regime. Further discussions of the history and significance of transonic flows can be found in the books by Anderson, e.g.,[5] and [7].

Transonic flow is characterized by non-negligible nonlinearity and is governed by equations of mixed type, even if thin wings or airfoils are considered. Perhaps the simplest equation governing transonic flow is the transonic small disturbance equation (TSDE)

$$(M^2 - 1)\phi_{xx} \approx \phi_{yy}, \tag{1.1}$$

which is typically valid for near-sonic flow ($M \approx 1$) over thin two dimensional wings or turbine blades. Here M is the local value of the Mach number given by

$$M^2 - 1 \approx M_\infty^2 - 1 + 2\tilde{\Gamma}_\infty \phi_x, \tag{1.2}$$

where M_∞ is the freestream (or undisturbed) Mach number, x and y are the spatial coordinates, and $\phi = \phi(x, y)$ is the disturbance potential related to the full velocity potential Φ by

$$\Phi \equiv Ux + \phi. \tag{1.3}$$

The quantity U is the undisturbed or free stream flow velocity, and $\tilde{\Gamma}$ is the non-dimensional

fundamental derivative evaluated at the undisturbed, or free stream, conditions. The scaled fundamental derivative is related to the dimensional fundamental derivative Γ by

$$\tilde{\Gamma} \equiv \frac{\rho}{a}\Gamma, \tag{1.4}$$

where

$$\Gamma \equiv \Gamma(\rho, s) \equiv \frac{a}{\rho} + \left.\frac{\partial a}{\partial \rho}\right|_s \tag{1.5}$$

and

$$a \equiv a(\rho, s) \equiv \left(\left.\frac{\partial P}{\partial \rho}\right|_s\right)^{\frac{1}{2}} \tag{1.6}$$

is the thermodynamic sound speed, $P = P(\rho, s)$ is the thermodynamic pressure, ρ is the fluid density, and s is the fluid entropy.

Inspection of (1.1) and (1.2) reveals that the fundamental derivative is the parameter characterizing the basic gasdynamic nonlinearity of the problem. The fact that Γ is a measure of the gasdynamic nonlinearity is also evident by inspection of (1.5), which defines Γ as the rate of change of the sound speed with density. It is the variations in the convected sound speed which gives rise to all of the nonlinearity in compressible inviscid flow. An alternate form of (1.5) can be derived by a simple change in variables from ρ to the specific volume

$$V = \frac{1}{\rho}$$

to yield

$$\Gamma = \left.\frac{V^4}{2a}\frac{\partial^2 P}{\partial V^2}\right|_s, \tag{1.7}$$

which is completely equivalent to (1.5). From (1.7), we see that we can interpret the fundamental derivative as being proportional to the curvature of isentropes in a $P-V$ plane. Thus Γ is a measure of the deviation of the stress-stain relation from a linear $P-V$ relation. As a result, we can think of the fundamental derivative as a measure of the material nonlinearity. Further, easily accessible discussions of the role of the fundamental derivative can be found in [9], [10], [12], and [11].

We note that we can recover a more familiar form (1.5) and (1.2) by recognizing that

$$\tilde{\Gamma} = \frac{\rho\Gamma}{a} = \frac{\gamma+1}{2} \tag{1.8}$$

for perfect gasses. Here γ is the ratio of specific heats. From the condition of a stable thermodynamic equilibrium, $\gamma > 1$ and $\tilde{\Gamma} > 1$ for all fluids in the perfect gas limit. Thus, in the perfect gas theory, there is always a lower bound of the nondimensional material nonliniearity parameter $\tilde{\Gamma}$.

It is easily demonstrated that the TSDE (1.1) is of an elliptic type whenever the flow is locally subsonic, i.e, $M < 1$, and is hyperbolic whenever the local flow is supersonic, i.e, $M > 1$. The challenge of computing transonic flow is directly related to the fact that the flow is not only of mixed type, but that the regions of hyperbolic and elliptic character are part of the final solution. The nonlinearity represented by the second term on the right hand side of (1.2) not only generates shock waves in the hyperbolic regions, but is the mechanism by which the flow changes type.

Because of the nonlinearity and mixed type, very few analytical solutions are available. The first to develop numerical solutions to transonic flow was [1], who solved (1.1) and (1.2) using the successive line relaxation (SLR) scheme. The primary new feature was that a switch was introduced in order to change the differencing from central differencing in the elliptic ($M < 1$) regions to backward differencing in the hyperbolic ($M > 1$) regions. Since that time, a number of researchers have developed codes based on the original idea developed in [1]. As computer speeds and memory increased, schemes based on the full potential equation, the Euler equations, and the full Navier-Stokes equations have been developed as can be seen in [5].

In much of the previous research, the equation of state was taken to be the perfect gas model. However, stationary power plants typically operate in the high pressure regimes of their working fluid. At such high pressure, the ideal gas equation of state is no longer valid and one must employ considerably more sophisticated equation of state, e.g, extensions of the Van der Waals equations of state. One of the most interesting effects of fluid pressurization is that the fundamental derivative (1.4)-(1.5) decreases and can even become negative. Examples of the variation of Γ with density are provided in Figure 1.1. Thus the material nonlinearity represented by (1.4)-(1.5) can be much smaller than the nonlinearity of gases in the low pressure limit.

The main focus of the present study is to examine the transonic dynamics of fluids having $\Gamma < 0$ for a range of pressures and temperatures in the single-phase regime. Such fluids are called Bethe-Zel'dovich-Thompson (BZT) fluids in honor of the scientists who first described such fluids. When $\Gamma < 0$, compression shocks violate the entropy inequality and cannot exist; see, e.g., [12] and [10]. If a compression discontinuity is inserted in a $\Gamma < 0$ fluid, it disintegrates into a centered compression fan. In addition, the only shock satisfying the entropy inequality when $\Gamma < 0$ are expansion shocks. From the point of view of the aerodynamics of power systems, this means that the strength of the adverse pressure gradients associated with

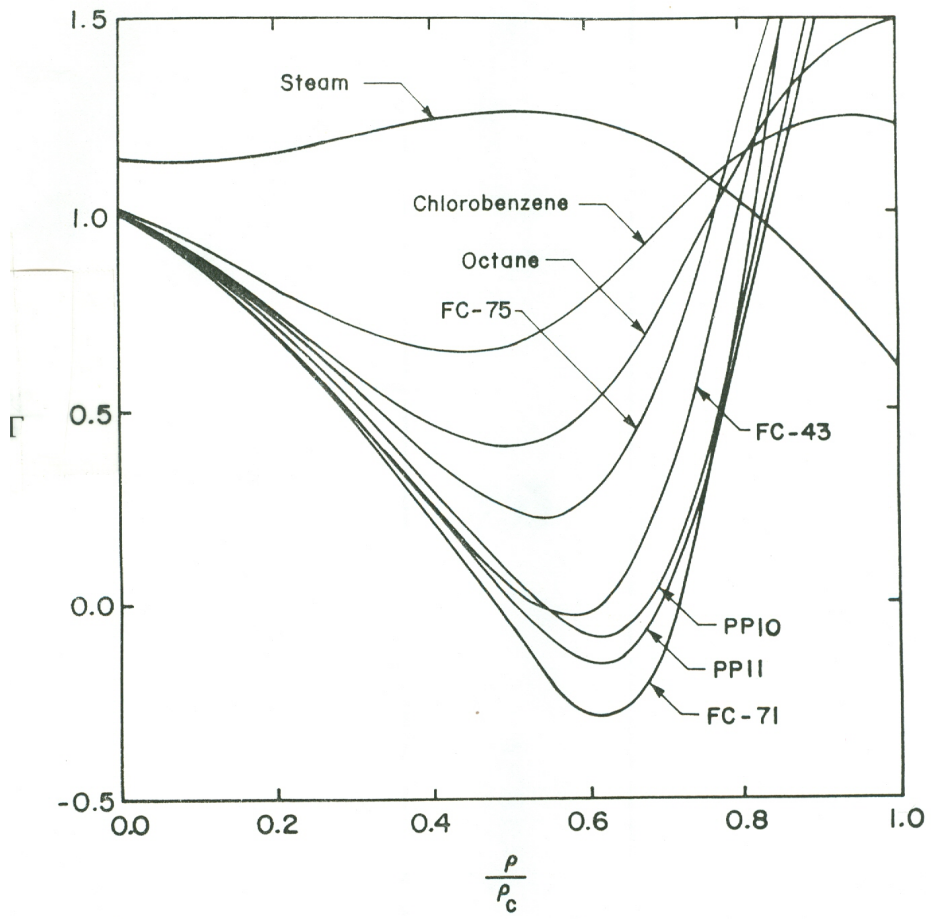

Figure 1.1: Variation of the fundamental derivative with density

compression shocks is reduced from infinity to a bounded and moderate values, resulting in a suppression of separation through the natural dynamics of BZT fluids. An example of such a suppression has been provided by [13].

Another advantage of pressurized and BZT fluids is that the reduced nonlinearity will narrow the range of Mach numbers corresponding to transonic flow. For example, the critical Mach number, i.e., the free stream Mach number at which the local Mach number first becomes unity, can be estimated as

$$M_{critical} \approx 1 - \frac{1}{2}[\tilde{\Gamma}_\infty |C_{p_{inc}}\Big|_{min}|]^{\frac{2}{3}}, \tag{1.9}$$

where $C_{p_{inc}}\Big|_{min} < 0$ is the minimum pressure coefficient over the wing or turbine blade of interest at $M_\infty = 0$. Thus, as $\tilde{\Gamma}_\infty \to 0$, $M_{critical} \to 1$ suggesting that the transonic zone will

vanish. Further examples of the increase in the critical Mach number have been provided by [3].

The first to compute external transonic flows of BZT fluids was Morren, e.g., [14] and [15], who used a finite volume approach to solve the Euler equations with a Van der Waals equation of state. Morren showed that expansion shocks are naturally captured by the scheme. In fact, Morren demonstrated that both expansion and compression shocks can appear on the wing. Significant increases in the lift to wave drag ratio were also described. Since Morren's work, others have extended her work to include more sophisticated and complex equations of state; see, [16], [18], [17], [19], and [21]. Further calculations using the full Navier-Stokes (N-S) equations have been carried out by [20].

The purpose of our work is to use a similar computational scheme as one used by [1] to examine flows of gasses with $\tilde{\Gamma}$ close to zero. After the non-classical Transonic Small Disturbance Equation is derived, as described later , it will be examined computationally and graphically. In the end it will be demonstrated that by examining the free stream conditions of the gas in question, a qualitative, and sometime quantitative, behavior of the flow over an airfoil can be predicted. The analysis includes subsonic and supersonic free stream velocities.

Chapter 2

Formulation

The derivation of the Full Potential equation that is needed to develop the TSDE follows the Navier Stokes theory with several assumptions, i.e., the fluid is inviscid and there are no body forces or energy sources. After these assumptions, the resulting equations are recognized as the Euler equations in the following form,

$$\frac{D\rho}{Dt} + \rho\nabla \cdot \mathbf{v} = 0 \tag{2.1}$$

$$\frac{D\mathbf{v}}{Dt} + \frac{\nabla P}{\rho} = \mathbf{0} \tag{2.2}$$

$$\frac{Ds}{Dt} = 0. \tag{2.3}$$

Here $\mathbf{v}$ is the velocity vector of a fluid particle. Since any state variable can be expressed in terms of any two other state variables, $P = P(\rho, T) = P(\rho, s)$. The boundary conditions used in the development of the potential equation are

$$\begin{gathered} \mathbf{v}_\infty \to \mathbf{U}_\infty, \\ \rho, s \to \rho_\infty, s_\infty = constant, \end{gathered} \tag{2.4}$$

where ∞ represents values infinitely far away, i.e, $|\mathbf{x}| \to \infty$. Here $\mathbf{U}_\infty$ is the constant velocity, ρ_∞ is the density , and s_∞ is the entropy as $|\mathbf{x}| \to \infty$. These are known as the free stream conditions.

For the following analysis, it should be noted that the gas dynamics satisfy the thermodynamic stability criteria, that is,

$$c_v \equiv \left.\frac{\partial e}{\partial T}\right|_\rho = T\left.\frac{\partial s}{\partial T}\right|_\rho \geq 0$$

and

$$c_p \equiv \left.\frac{\partial h}{\partial T}\right|_P = T\left.\frac{\partial s}{\partial T}\right|_P > c_v \geq 0$$

for all N-S fluids. Here, $h = e + PV$ is the enthalpy, e is the internal energy, and T is absolute temperature. The above are well known definitions of specific heats at constant density and pressure respectively. These conditions satisfy the fact that entropy, s, cannot decrease. As previously stated,

$$\gamma = \frac{c_p}{c_v} > 1 \tag{2.5}$$

for all fluids.

We now rewrite (1.6) as

$$a^2 = \left.\frac{\partial P}{\partial \rho}\right|_s = \gamma\left.\frac{\partial P}{\partial \rho}\right|_T. \tag{2.6}$$

Because of (2.5), it can be concluded that (2.6) is always greater than zero, and, therefore, (1.6) is real for all N-S fluids. This also indicates that the slope of the isentropes is always negative in the P-V diagram.

Chapter 3

Full Potential Equation

To develop the Full Potential Equation, further assumptions are made, i.e., the flow is steady, irrotatioinal, and isentropic. The well known exact boundary conditions for potential flow are

$$\begin{cases} \phi_y = (U + \phi_x)\epsilon\dot{f}(\frac{x}{L}) & on\ y = \epsilon L f(\frac{x}{L}) \\ \phi_y = 0 & on\ y = 0 \\ \phi \to 0 & as\ |\mathbf{x}| \to \infty \\ \rho \to \rho_\infty & as\ |\mathbf{x}| \to \infty, \end{cases} \tag{3.1}$$

where L is the chord length of a wing, ϵ is the ratio of thickness to chord length, and f and $\dot{f}$ are the equation of the wing shape and its derivative in terms of $\frac{x}{L}$ respectively. Here, $\mathbf{U}$ is now taken to be uniform and parallel to the x-axis, which is represented by U. Figure 3.1 shows an example of the boundary conditions including a wing shape. In our case, only the top half of the wing is considered, which corresponds to the equation of the wing shape, i.e., f.

We begin with enthalpy $h \equiv e + PV$ and the Gibbs' Relation

$$Tds = de + PdV. \tag{3.2}$$

Gibbs' Relation, (3.2), can be rewritten as $dh = Tds + VdP$. In vector form we may write this as

$$\nabla h = T\nabla ds + V\nabla P. \tag{3.3}$$

The linear momentum (2.2) can be rewritten as

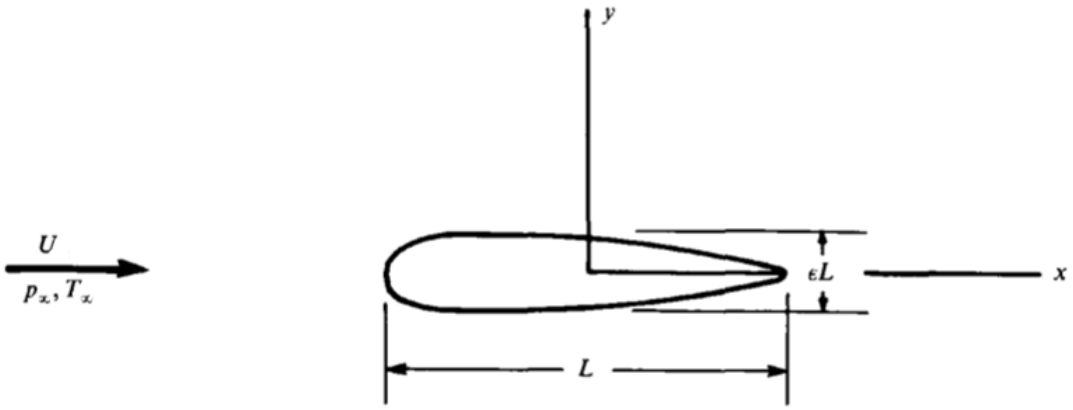

Figure 3.1: Wing shape of a NACA 00XX wing with free stream conditions of U, ρ_∞, and T_∞.

$$\frac{\partial \mathbf{v}}{\partial t} + \nabla(\frac{|\mathbf{v}|^2}{2} + h) + \boldsymbol{\zeta} \times \mathbf{v} = T\nabla s \tag{3.4}$$

by expanding the substantial derivative $\frac{D\mathbf{v}}{Dt} = \frac{\partial \mathbf{v}}{\partial t} + \mathbf{v} \cdot \nabla \mathbf{v}$, using the vector identity $\mathbf{v} \cdot \nabla \mathbf{v} = \nabla(\frac{\mathbf{v^2}}{\mathbf{2}}) + \boldsymbol{\zeta} \times \mathbf{v}$ where $\boldsymbol{\zeta} \equiv \nabla \times \mathbf{v}$ is the vorticity, and utilizing (3.3).

Since the flow is irrotational, i.e, $\boldsymbol{\zeta} = \mathbf{0}$ and $\mathbf{v} = \nabla\Phi$, (3.4) becomes

$$\nabla(h + \frac{\partial \Phi}{\partial t} + \frac{|\mathbf{v}|^2}{2}) = T\nabla s. \tag{3.5}$$

By imposing our steady and isentropic flow assumptions, (3.5) becomes

$$\nabla(h + \frac{|\mathbf{v}|^2}{2}) = \mathbf{0}. \tag{3.6}$$

The exact solution to (3.6) is

$$h + \frac{|\mathbf{v}|^2}{2} = B, \tag{3.7}$$

where B is a constant. If we now impose the condition of a constant flow upstream of the wing or body, i.e., (2.4), we find (3.7) becomes

$$h + \frac{|\mathbf{v}|^2}{2} = h_\infty + \frac{U^2}{2}, \tag{3.8}$$

which is the Bernoulli equation for steady, isentropic, and irrotational flow. Keeping in mind the steady and irrotational conditions, (2.2) can be written as

$$\nabla \frac{|\mathbf{v}|^2}{2} + \frac{\nabla P}{\rho} = \mathbf{0}. \tag{3.9}$$

Taking the gradient of the equation of state $P = P(\rho, s)$ results in

$$\nabla P = \left.\frac{\partial P}{\partial \rho}\right|_s \nabla \rho + \left.\frac{\partial P}{\partial s}\right|_\rho \nabla s.$$

Substituting (1.6) into the above and again assuming isentropic flow, the equation reduces to

$$\nabla P = a^2 \nabla \rho.$$

If we substitute into (3.9) then dot the result with the velocity vector, we attain

$$\mathbf{v} \cdot \nabla \rho = -\frac{\rho}{a^2} \mathbf{v} \cdot \nabla (\frac{|\mathbf{v}|^2}{2}). \tag{3.10}$$

Equation (3.10) can be substituted into (2.1) after the substantial derivative in (2.1) is expanded. After rearranging and substituting in $\mathbf{v} = \nabla \Phi$, the result is

$$\nabla \Phi \cdot \nabla (\frac{|\nabla \Phi|^2}{2}) = a^2 \nabla^2 \Phi. \tag{3.11}$$

This is the Full Potential Equation, which depends on ρ through $a = a(\rho, s)$. Because $a^2 = a^2(\rho, s_\infty)$, we close the system by combining (3.11) with (3.8), which yields two scalar equations for Φ and ρ.

Chapter 4

Universal Transonic Small Disturbance Equation

We now convert the derived Full Potential Equation (3.11) to operate under the small disturbance condition in transonic regimes by imposing $\epsilon << 1$, $M_\infty - 1 \approx 0$, and by taking the flow to be two dimensional so that the z dependence can be ignored. In two dimensions, (3.11) can then be rewritten as

$$(\Phi_x^2 - a^2)\Phi_{xx} + 2\Phi_x\Phi_y\Phi_{xy} + (\Phi_y^2 - a^2)\Phi_{yy} = 0. \tag{4.1}$$

If we write the Mach number in terms of velocity potentials, we have

$$M^2 = \frac{\Phi_x^2 + \Phi_y^2}{a^2}. \tag{4.2}$$

If we solve for Φ_x^2 then substitute (4.2) into the first term of (4.1), we have

$$(M^2 - 1)\Phi_{xx} - \frac{\Phi_y^2}{a^2}\Phi_{xx} + \frac{2\Phi_x\Phi_y}{a^2}\Phi_{xy} = (1 - \frac{\Phi_y^2}{a^2})\Phi_{yy}. \tag{4.3}$$

Substituting (1.3) and its derivatives into (4.3) leads to

$$(M^2 - 1)\phi_{xx} - \frac{\phi_y^2}{a^2}\phi_{xx} + \frac{2(U + \phi_x)\phi_y}{a^2}\phi_{xy} = (1 - \frac{\phi_y^2}{a^2})\phi_{yy}\ . \tag{4.4}$$

We now introduce the scaled perturbation variables as

$$\begin{aligned} \phi &= UL\alpha\bar{\phi}, \\ \bar{a} &= \tfrac{a}{a_\infty} \approx 1, \\ x &= L\bar{x}, \\ y &= \tfrac{L\hat{y}}{\delta}, \end{aligned} \tag{4.5}$$

where $\bar{\phi}, \bar{a}, \bar{x}$, and $\hat{y}$ are non-dimensional variables of $O(1)$, and δ and α are small non-dimensional numbers. The y coordinate has a δ term in the denominator because the flow is transonic, and therefore, the Mach lines are almost vertical. This means that the disturbance is felt very far away from the wing in the vertical direction. The δ stretches the non-dimensional $\hat{y}$ variable into a physical y.

Differentiating (4.5) with respect to the appropriate variables, substituting into (4.4), then rearranging leads to

$$\frac{(M^2-1)}{\delta^2}\bar{\phi}_{\bar{x}\bar{x}} - \alpha^2\bar{\phi}_{\hat{y}}^2\bar{\phi}_{\bar{x}\bar{x}} + 2\alpha\bar{\phi}_{\hat{y}}\bar{\phi}_{\bar{x}\hat{y}} + 2\alpha^2\bar{\phi}_{\hat{y}}\bar{\phi}_{\bar{x}}\bar{\phi}_{\bar{x}\hat{y}} = \bar{\phi}_{\hat{y}\hat{y}} - \alpha^2\delta^2\bar{\phi}_{\hat{y}}^2\bar{\phi}_{\hat{y}\hat{y}} \ ,$$

where we have used $U \approx a_\infty$ for transonic flows and $\bar{a} \approx 1$ for small disturbance. With α small and δ^2 balancing $M^2 - 1$ the equation reduces to

$$\frac{(M^2-1)}{\delta^2}\bar{\phi}_{\bar{x}\bar{x}} \approx \bar{\phi}_{\hat{y}\hat{y}} \ . \tag{4.6}$$

If $\delta = 1$, meaning the y coordinate is not stretched, $\frac{M^2-1}{\delta^2} \approx 0$, leaving $\bar{\phi}_{\hat{y}\hat{y}} \approx 0$. This does not have a valid solution because the boundary conditions at the wing and at the far field cannot be met simultaneously.

Chapter 5

Non-classical Transonic Small Disturbance Equation

By enforcing isentropic flow, by differentiating (3.8) with respect to ρ, and utilizing (3.3), the equation for the Mach number on an isentrope in terms of the non-dimensional fundamental derivative $\tilde{\Gamma}$ and ρ can be written as

$$\frac{dM^2}{d\rho} = \frac{2}{\rho}(M^2 - 1 - \tilde{\Gamma}M^2). \tag{5.1}$$

As previously discussed, $\tilde{\Gamma}$ is very close to zero for a BZT gas. To capture this feature, the $\tilde{\Gamma}$ curve is designed to be a shallow concave up parabola with a local minimum slightly below the x-axis and with first derivatives on the x-axis to be very small. This mimics some of the curves seen in Figure 1.1. If we expand $\tilde{\Gamma}$ around the free stream ρ_∞ in a Taylor series, we find

$$\tilde{\Gamma} = \frac{\rho a_\infty}{\rho_\infty a}[\tilde{\Gamma}_\infty + \Lambda_\infty(\frac{\rho - \rho_\infty}{\rho_\infty}) + \frac{\Xi_\infty}{2}(\frac{\rho - \rho_\infty}{\rho_\infty})^2 + O(\frac{\rho - \rho_\infty}{\rho_\infty})^3]. \tag{5.2}$$

The ratio $\frac{\rho a_\infty}{\rho_\infty a} \approx 1$ for transonic flow and

$$\begin{aligned} \Lambda_\infty &\equiv \frac{\rho_\infty^2}{a_\infty}\frac{\partial\Gamma(\rho_\infty, a_\infty)}{\partial\rho}\bigg|_s, \\ \Xi_\infty &\equiv \frac{\rho_\infty^3}{a_\infty}\frac{\partial^2\Gamma(\rho_\infty, a_\infty)}{\partial\rho^2}\bigg|_s, \end{aligned} \tag{5.3}$$

where we require that $\Lambda_\infty = O(\frac{\rho-\rho_\infty}{\rho_\infty})$ and $\Xi_\infty = O(1)$. To satisfy (5.2) and to acquire the parabola shape of the $\tilde{\Gamma}$ curve , $\tilde{\Gamma}$ needs to be of $O(\frac{\rho-\rho_\infty}{\rho_\infty})^2$ to balance the higher order terms,

which forces $\tilde{\Gamma}$ to be close to zero as desired. For a low pressure gas, where $\tilde{\Gamma}$ is of O(1), (5.2) would take the form $\tilde{\Gamma} \approx \tilde{\Gamma}_\infty$ because the first term of (5.2) would dominate the other terms and, therefore, would lead to $\tilde{\Gamma} \approx \tilde{\Gamma}_\infty \approx$ *constant*.

Substituting (5.2) into (5.1) then integrating between $M_\infty, \rho_\infty \to M, \rho$ leads to

$$M^2 - 1 = (M_\infty^2 - 1) - 2\tilde{\Gamma}_\infty(\frac{\rho - \rho_\infty}{\rho_\infty}) - \Lambda_\infty(\frac{\rho - \rho_\infty}{\rho_\infty})^2 - \frac{\Xi_\infty}{3}(\frac{\rho - \rho_\infty}{\rho_\infty})^3 + O(\frac{\rho - \rho_\infty}{\rho_\infty})^4 + O[(M^2 - 1)(\frac{\rho - \rho_\infty}{\rho_\infty})].$$

Since every term in the expression is $O(\frac{\rho-\rho_\infty}{\rho_\infty})^3$, $M_\infty^2 - 1$ needs to be $O(\frac{\rho-\rho_\infty}{\rho_\infty})^3$ to be balanced with the other terms. In the last term on the right, $M^2 - 1 \approx M_\infty^2 - 1 = O(\frac{\rho-\rho_\infty}{\rho_\infty})^3$ therefore $(M^2 - 1)(\frac{\rho-\rho_\infty}{\rho_\infty}) = O(\frac{\rho-\rho_\infty}{\rho_\infty})^4$. Removing $O(\frac{\rho-\rho_\infty}{\rho_\infty})^4$ terms leaves

$$M^2 - 1 \approx (M_\infty^2 - 1) - 2\tilde{\Gamma}_\infty(\frac{\rho - \rho_\infty}{\rho_\infty}) - \Lambda_\infty(\frac{\rho - \rho_\infty}{\rho_\infty})^2 - \frac{\Xi_\infty}{3}(\frac{\rho - \rho_\infty}{\rho_\infty})^3. \tag{5.4}$$

By once again imposing the isentropic condition and writing $h - h_\infty$ as a first order Taylor expansion results in

$$h - h_\infty = \left.\frac{\partial h}{\partial \rho}\right|_s (\rho - \rho_\infty) + O(\rho - \rho_\infty)^2. \tag{5.5}$$

Then rearranging (3.2) leads to

$$\left.\frac{\partial h}{\partial \rho}\right|_s = \frac{1}{\rho}\left.\frac{\partial P}{\partial \rho}\right|_s = \frac{a^2}{\rho}. \tag{5.6}$$

By utilizing (5.5), (5.6), and (3.8), substituting the small disturbance variables, and combining terms leads to

$$\frac{a_\infty^2}{\rho_\infty}(\rho - \rho_\infty) = -U\phi_x - \frac{1}{2}(\phi_x^2 + \phi_y^2) + O(\rho - \rho_\infty)^2$$

The first term on the right side can be shown to be much larger than the second because of U. Eliminating the second term on the right, rearranging, then writing in terms of non-dimensional variables results in

$$\frac{\rho - \rho_\infty}{\rho_\infty} \approx -M_\infty^2 \alpha \bar{\phi}_x. \tag{5.7}$$

Substituting (5.4) into (4.6), then substituting (5.7) into the result gives the non-dimensional Non-classical Transonic Small Disturbance Equation

$$[\frac{M_\infty^2 - 1 + 2\tilde{\Gamma}_\infty M_\infty^2 \alpha \bar{\phi}_{\bar{x}} - \Lambda_\infty M_\infty^4 \alpha^2 \bar{\phi}_{\bar{x}}^2 + \frac{\Xi_\infty}{3} M_\infty^6 \alpha^3 \bar{\phi}_{\bar{x}}^3}{\delta^2}]\bar{\phi}_{\bar{x}\bar{x}} = \bar{\phi}_{\hat{y}\hat{y}}. \tag{5.8}$$

Combining (4.5) and (3.1), the non-dimensional boundary conditions are transformed to

$$\begin{cases} \bar{\phi}_{\hat{y}} = \frac{\epsilon}{\alpha\delta}\dot{f}(\bar{x}) & on \;\; \hat{y} = 0 \; on \; the \; wing \\ \bar{\phi}_{\hat{y}} = 0 & on \;\; \hat{y} = 0 \; off \; the \; wing \\ \bar{\phi} \to 0 & as \;\; |\bar{x}| \to \infty. \end{cases} \tag{5.9}$$

For convenience, we set

$$\begin{aligned} \tfrac{\tilde{\Gamma}_\infty M_\infty^2 \alpha}{\delta^2} &= 1, \\ \hat{\Gamma}_\infty &= \tfrac{\tilde{\Gamma}_\infty}{\alpha^2}, \\ \hat{\Lambda}_\infty &= \tfrac{\Lambda_\infty}{\alpha}, \\ \tfrac{\epsilon}{\alpha\delta} &= sign(\Gamma_\infty), \end{aligned} \tag{5.10}$$

where $\hat{\Gamma}_\infty$ and $\hat{\Lambda}_\infty$ are of $O(1)$. Using (5.10), (5.8) can be written as

$$(-K_1 + 2\bar{\phi}_{\bar{x}} - K_2\bar{\phi}_{\bar{x}}^2 + \frac{K_3}{3}\bar{\phi}_{\bar{x}}^3)\bar{\phi}_{\bar{x}\bar{x}} = \bar{\phi}_{\hat{y}\hat{y}}, \tag{5.11}$$

and (5.9) can be written as

$$\begin{cases} \bar{\phi}_{\hat{y}} = sign(\Gamma_\infty)\dot{f}(\bar{x}) & on \;\; \hat{y} = 0 \; on \; the \; wing \\ \bar{\phi}_{\hat{y}} = 0 & on \;\; \hat{y} = 0 \; off \; the \; wing \\ \bar{\phi} \to 0 & as \;\; |\bar{x}| \to \infty, \end{cases} \tag{5.12}$$

with

$$
\begin{aligned}
K_1 &= \tfrac{1-M_\infty^2}{(\epsilon^3|\hat{\Gamma}_\infty|M_\infty^2)^{\frac{2}{5}}}, \\
K_2 &= \tfrac{\hat{\Lambda}_\infty}{\hat{\Gamma}_\infty} M_\infty^2, \\
K_3 &= \tfrac{\Xi_\infty}{\hat{\Gamma}_\infty} M_\infty^4, \\
\alpha &= \left(\tfrac{\epsilon^2}{M_\infty^2|\hat{\Gamma}_\infty|} \right)^{\frac{1}{5}} sign(\hat{\Gamma}_\infty), \\
\delta &= (\epsilon^3 M_\infty^2 |\hat{\Gamma}_\infty|)^{\frac{1}{5}}.
\end{aligned}
\tag{5.13}
$$

With dense gasses with very low $\tilde{\Gamma}$, the free stream Mach numbers are very close to one, therefore it is reasonable to set $M_\infty = 1$ in the above parameters as long as there is no loss in accuracy, i.e., $1 - M_\infty^2$ in the K_1 parameter will result in 0, meaning the substitution into this term would lead to a non-sensible result.

Because $M^2 - 1 = O(\delta^2)$, from (5.13) we have $M^2 - 1 = O(\epsilon^{\frac{6}{5}})$, which is much less than the Mach number range of $\epsilon^{\frac{2}{3}}$ found in the case of classical ($\tilde{\Gamma}_\infty = O(1)$) transonic flow. Thus, the small values of the fundamental derivative used here results in a considerable narrowing of the range of Mach numbers corresponding to transonic flow. This order of magnitude result is consistent with the comments of Chapter 1 regarding the increase in critical Mach number when $\tilde{\Gamma}_\infty$ is small.

From (4.5) and (5.13), we also conclude that the disturbances extend a distance of $\frac{L}{\delta} = O(\frac{L}{\epsilon^{\frac{3}{5}}})$ which is considerably further from the airfoil than that of the classical ($\tilde{\Gamma}_\infty = O(1)$) theory; the latter distance is $O(\frac{L}{\epsilon^{\frac{1}{3}}})$.

The non-classical transonic small disturbance equation, (5.11), can be written in conservative form as

$$
\frac{\partial F}{\partial \bar{x}} + \frac{\partial G}{\partial \hat{y}} = 0, \tag{5.14}
$$

where

$$
F = K_1 \hat{\rho} + \hat{\rho}^2 + \frac{K_2}{3} \hat{\rho}^3 + \frac{K_3}{12} \hat{\rho}^4 \tag{5.15}
$$

and $G = -\bar{\phi}_{\hat{y}}$. By rearranging (5.7), $\hat{\rho}$ is defined as

$$\hat{\rho} \approx -\bar{\phi}_{\bar{x}} \approx \frac{C_p}{2\alpha} \approx \frac{\rho - \rho_\infty}{\rho_\infty \alpha} = O(1). \tag{5.16}$$

Taking derivatives of (5.15) with respect to $\hat{\rho}$ results in

$$F' = K_1 + 2\hat{\rho} + K_2\hat{\rho}^2 + \frac{K_3}{3}\hat{\rho}^3 = \frac{1 - M^2}{\delta^2}, \tag{5.17}$$

and

$$F'' = 2[1 + K_2\hat{\rho} + \frac{K_3}{2}\hat{\rho}^2] = 2\frac{\tilde{\Gamma}_{local}}{\tilde{\Gamma}_\infty}. \tag{5.18}$$

Through personal communication with M.S. Cramer,March 10, 2013, it was determined that F, called the flux function, is essentially the image of the isentrope which passes through the free stream state. As in the classical $\tilde{\Gamma}_\infty = O(1)$ theory, the shock adiabat is coincident with the isentrope, at least to the accuracy required here. Thus, $F = F(\hat{\rho})$ can be regarded as both the isentrope and the shock adiabat going through the free stream state.

A typical shape of the flux function of interest can be seen in Figure 5. The free stream condition lies on the origin, $\hat{\rho} = 0$, $F = 0$. Equation (5.17) was developed using (5.4) and the conditions previously stated. Thus, the slope of the flux function F is the measure of the local Mach number. This means that if the slope is negative, the flow is supersonic, and vise verse. The second derivative of F is the measure of the local value of $\tilde{\Gamma}$. Where the F curve is concave down, $\tilde{\Gamma}$ is negative, and vise verse.

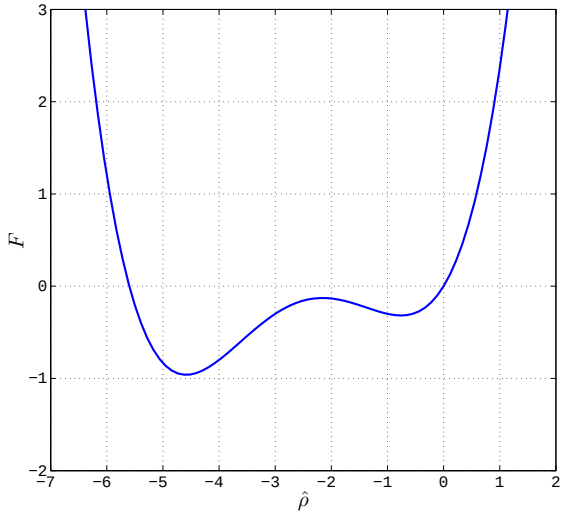

Figure 5.1: Typical shape of the F curve. The value of $K_1 = 1$, $K_2 = 1$, and $K_3 = 0.4$

Chapter 6

Shocks and Shock Existence

The shock jump conditions associated with (5.14) can be derived by a number of means. One approach is to apply a perturbation technique, similar to that used in the present thesis, to the Rankine-Hugoniot jump conditions and fundamental existence conditions for shock waves. Alternatively, we could require that (5.14) be consistent with a more general dissipative theory. This is, any admissible shock wave should have a sufficiently smooth dissipative structure governed by the dissipative extension of (5.14), i.e.,

$$\frac{\partial F}{\partial \bar{x}} + \frac{\partial G}{\partial \hat{y}} = -\nu \bar{\phi}_{\bar{x}\bar{x}\bar{x}}, \tag{6.1}$$

where $\nu \geq 0$ is a small dissipation constant. We note that (6.1) is exactly the extension of the TSDE for weak dissipation and weak thermal conduction. The term on the right hand side is also of the same form as that used as explicit dissipation in our numerical computations. We re-write (6.1) as

$$\begin{array}{c} G_{\hat{y}} + F_{\bar{x}} = -\nu \hat{\rho}_{\bar{x}\bar{x}} \\ \hat{\rho}_{\hat{y}} - G_{\bar{x}} = 0, \end{array} \tag{6.2}$$

where (5.16) has been used. The second of (6.2) is recognized as the compatibility or irrotationality condition. If we carry out a standard shock structure analysis on (6.2), we find that the shock jump conditions corresponding to (5.11) are

$$\hat{\sigma}^2 = \left(\frac{d\bar{x}}{d\hat{y}}\bigg|_{shock}\right)^2 = -\frac{[\![F]\!]}{[\![\hat{\rho}]\!]} \tag{6.3}$$

and

$$[\![G]\!] = -\hat{\sigma}[\![\hat{\rho}]\!], \tag{6.4}$$

where $\hat{\sigma}$ is a scaled shock angle measured from the positive $\hat{y}$ axis, i.e.,

$$\hat{\sigma} = (\frac{d\bar{x}}{d\hat{y}}\bigg|_{shock}), \tag{6.5}$$

The notation $[\![.]\!]$ signifies a jump in a value. The physical shock angle, measured from the positive y axis, is

$$\sigma \equiv \delta\hat{\sigma} = O(\delta). \tag{6.6}$$

From (6.3) we can conclude that

$$\frac{[\![F]\!]}{[\![\hat{\rho}]\!]} \leq 0 \tag{6.7}$$

for all real shocks and that normal shocks ($\hat{\sigma} = 0$) correspond to

$$[\![F]\!] = 0. \tag{6.8}$$

As seen through personal communication with M.S. Cramer, July 01, 2013, condition (6.7) will be referred to as the condition of *geometric admissibility*. If we define a Rayleigh line as a straight line connecting any two points on the F *vs.* $\hat{\rho}$ curve, we can write

$$F_R = F_R(\hat{\rho}) \equiv F_i + \frac{[\![F]\!]}{[\![\hat{\rho}]\!]}(\hat{\rho} - \hat{\rho}_i) = F_i - \hat{\sigma}^2(\hat{\rho} - \hat{\rho}_i), \tag{6.9}$$

where $i = 1, 2$ indicate any intersection of the Rayleigh line with the F *vs.* $\hat{\rho}$ curve. Thus, all Rayleigh lines must have a negative slope in the $F - \hat{\rho}$ plane. We note that (6.9) can be shown to be the approximate form of the exact Rayleigh lines in the $P - V$ diagram, and can therefore be considered to be the states satisfying the jump condition from the normal momentum.

Jump condition (6.4) can also be written as

$$[\![\hat{\theta}]\!] = \hat{\sigma}[\![\hat{\rho}]\!], \tag{6.10}$$

where $\hat{\theta} \equiv \frac{\theta}{\delta\alpha}$ is a scaled version of the physical flow deflection angle θ and $G = -\bar{\phi}_{\hat{y}} = -\hat{\theta}$ has been used. Result (6.10) provides the relation among the flow deflection angle, shock angle, and shock strength.

The shock structure analysis of (6.2) can also be used to establish the physical shock existence conditions based on the idea that there must be a physically realizable transition between any proposed upstream and downstream states. It can be shown that the physical existence condition can be stated as follows:

A proposed discontinuity is an admissible $[\![\hat{\rho}]\!] \lessgtr 0$ *shock iff* $F \gtrless F_R$ *at every* $\hat{\rho}$ *between* $\hat{\rho}_1$ *and* $\hat{\rho}_2$.

Here the subscript 1 denotes the proposed upstream state and the subscript 2 denotes the proposed downstream state. That is, the Rayleigh line must be entirely above the F curve between the proposed upstream conditions for an admissible $[\![\hat{\rho}]\!] > 0$ shock and entirely below the F curve for an admissible $[\![\hat{\rho}]\!] < 0$ shock. A sample of a few Rayleigh lines of admissible shocks are depicted in Figure 6.1, where 1 and 2 again represent the upstream and downstream conditions respectively.

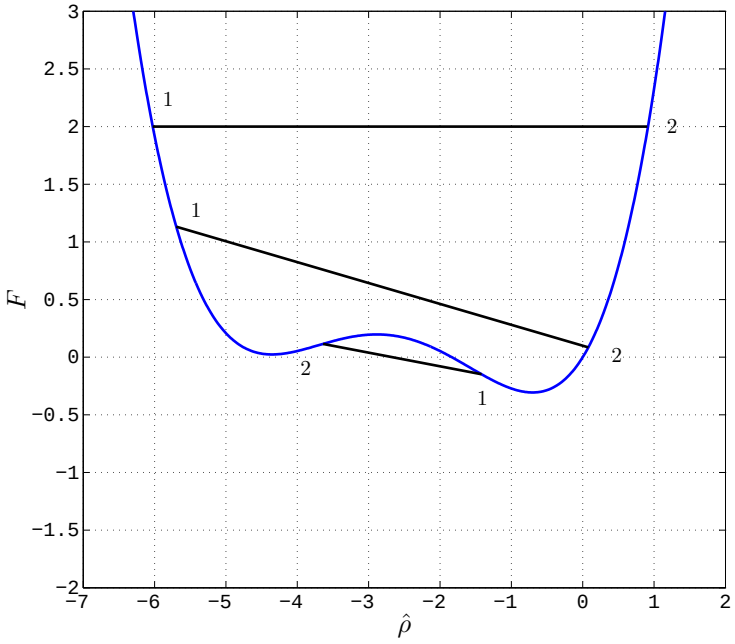

Figure 6.1: Example Rayleigh lines for admissible shock jumps directions. The lowest most Rayleigh line represents an expansion shock. The value of $K_1 = 1$, $K_2 = 0.9$, and $K_3 = 0.34$.

From (5.17) it can be shown that every admissible shock ($[\![F]\!] = 0$) takes the flow from supersonic to subsonic conditions. All admissible oblique shocks must always have supersonic conditions upstream and may or may not have subsonic conditions downstream. It was also shown through personal communication with M.S. Cramer, July 01, 2013, that all admissible shocks will result in an $O(\alpha^5)$ increase in entropy across the shock.

A type of shock which is not possible when $F = F(\hat{\rho})$ is convex corresponds to a Rayleigh lines which are tangent to the F *vs.* $\hat{\rho}$ curve. At such tangency points, the normal component of the Mach number is 1 and we refer to such shocks as sonic shocks. It can be verified that admissible shocks can be constructed which are sonic at either the upstream of downstream state. For the F curve sketched in Figures 6.1, one Rayleigh line can be constructed which is tangent at two points. This corresponds to the double sonic expansion shock first described by [12].

Sonic shocks also play a role in the partial disintegration of inadmissible discontinuities. For example, consider the proposed discontinuity from point 1 to 4 in Figure 6.2. The Rayleigh line $1 \rightarrow 4$ clearly intersects the F *vs.* $\hat{\rho}$ curve at points between 1 and 4 and is therefore inadmissible. However, an admissible transition from $1 \rightarrow 4$ can be constructed by shocking the flow through an oblique sonic shock (sonic at 2), from $1 \rightarrow 2$, an isentropic increase in $\hat{\rho}$, and then a sonic oblique shock from $3 \rightarrow 4$, which is sonic at the upstream state (3). Because the single proposed discontinuity breaks into two shocks, we refer to this phenomenon as shock-splitting.

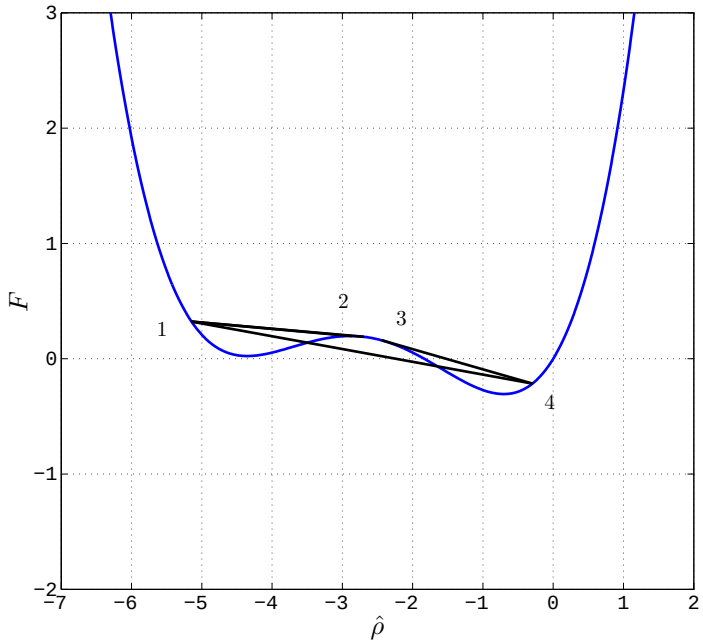

Figure 6.2: Example of Shock-Splitting. If the proposed discontinuity is $1 \rightarrow 4$, the shock splits into the oblique shock from $1 \rightarrow 2$, an isotropic compression, and the oblique shock from $3 \rightarrow 4$. The value of $K_1 = 1$, $K_2 = 0.9$, and $K_3 = 0.34$.

Chapter 7

Numerical Scheme

In order to solve the system described, a numerical scheme had to be used. The general method used is described in [1] and [2]. In this study the scheme was extended to supersonic free stream cases and an explicit artificial viscosity was added. The boundary value problem of the quasi-linear system is given by

$$(K_1 - K_{\frac{3}{2}}\bar{\phi}_{\bar{x}} + K_2\bar{\phi}_{\bar{x}}^2 - \frac{K_3}{3}\bar{\phi}_{\bar{x}}^3)\bar{\phi}_{\bar{x}\bar{x}} + \bar{\phi}_{\hat{y}\hat{y}} = -\nu\bar{\phi}_{\bar{x}\bar{x}\bar{x}}. \tag{7.1}$$

Here $K_{\frac{3}{2}} = 2$ when representing the classical and non-classical transonic behavior and $K_{\frac{3}{2}} = 0$ to recover the Laplace equation. Also, ν is the artificial viscosity parameter ranging between 10^{-5} and 10^{-2}. At times, to force the solution to converge, ν was picked to be quite large to compute the initial solution. Using the restart option, new solutions were calculated by using progressively lower ν. This was done until the result was virtually unchanged after the reduction in ν. The boundary value problem was solved on a rectangular domain $0 \leq \hat{y} \leq H$ and $\bar{x}_{min} \leq \bar{x} \leq \bar{x}_{max}$ with boundary conditions of

$$\begin{cases} \bar{\phi} = 0 & \bar{x} = \bar{x}_{min}, \bar{x}_{max} \\ \bar{\phi}_{\hat{y}} = 0 & \hat{y} = H \ (subsonic\ downstream) \\ \bar{\phi}_{\hat{y}} = -\sqrt{M_\infty - 1}\ \bar{\phi}_{\bar{x}} & \hat{y} = H \ (supersonic\ downstream) \end{cases} .$$

Here, H is the top boundary of the rectangular domain and $\bar{x}_{min}$ and $\bar{x}_{max}$ are the left (upstream) and right (downstream) boundary respectively. The supersonic free stream boundary conditions are those suggested by [4]. The boundary conditions at $\hat{y} \approx 0$ were

$$\begin{cases} \bar{\phi}_{\hat{y}} = sign(\Gamma_\infty)\dot{f} & -\frac{1}{2} \leq \bar{x} \leq \frac{1}{2} \\ \bar{\phi}_{\hat{y}} = 0 & otherwise \end{cases} ,$$

where $\dot{f}$ is the derivative of the wing shape f as stated before. The wing shapes examined

were a circular arc at 0^o of attack for validation and a NACA 00XX wing series for validation and our analysis. Because the angle of attack was 0^o in all of the cases, the solutions could be calculated on a half plane as in both [1] and [2].

The discretization of the partial differential equation was done by leaving the transonic equation, 7.1, in non-conservative form and simply substituting in the discritizations for each derivative as suggested by [5]. It was determined that the final form after finite difference discretization of the non-conservative and conservative equations, as in [6], was equivalent. This was determined through Taylor series analysis.

The system of equations was solved using the Successive Line Relaxation (SLR) scheme with the relaxation pararmeter $0 < \omega < 1$ for under-relaxation, and $1 < \omega < 2$ for over-relaxation. For solving Laplace's equation, the ideal value of $\omega = 1.9$. For transonic flow calculations, ω was typically taken to be below 1. The system was linearized by evaluating the $\bar{\phi}_x$ terms at the previous iteration. During each sweep the differencing changes depending on the Mach number of the flow at each point. This process is described in depth in [1]. The iterations were terminated when the average L_2 norm of the residual reached a specified tolerance. Absolute convergence was determined to be when the norm reached $5x10^{-3}$ or if the solution stopped changing significantly after several thousand iterations. The latter was prevalent in more complicated cases. During some calculations, ω was lowered in the middle of the iterations if the average L_2 norm leveled out above the tolerance. This forced the L_2 norm to drop, but usually did not change the solution significantly. The time and the amount of iterations to convergence varied greatly with the complexity of the case. When bow shocks or stern shocks were present, the solution on the wing converged much quicker than at the mentioned shocks; particularly the location of the bow and stern shocks.

The points on the wing were uniformly distributed. The amount of points for the results varied between 50-200. This is a large difference from the calculations done by [2] and [1]. We were able to use a large number of points because of the advances in computing power. For efficiency of computation, the grid was gradually stretched at the far field. The stretch ratio varied between 10% and 15% and the location of the beginning of the stretching was also specified depending on the amount of activity above the wing and in the far field. If an expansion shock was extremely close to the leading edge of the airfoil, clustering at that point was utilized. Figure 7.1 shows the kind of grid that was used for some of the calculations with significant activity above the wing and past the tail of the wing.

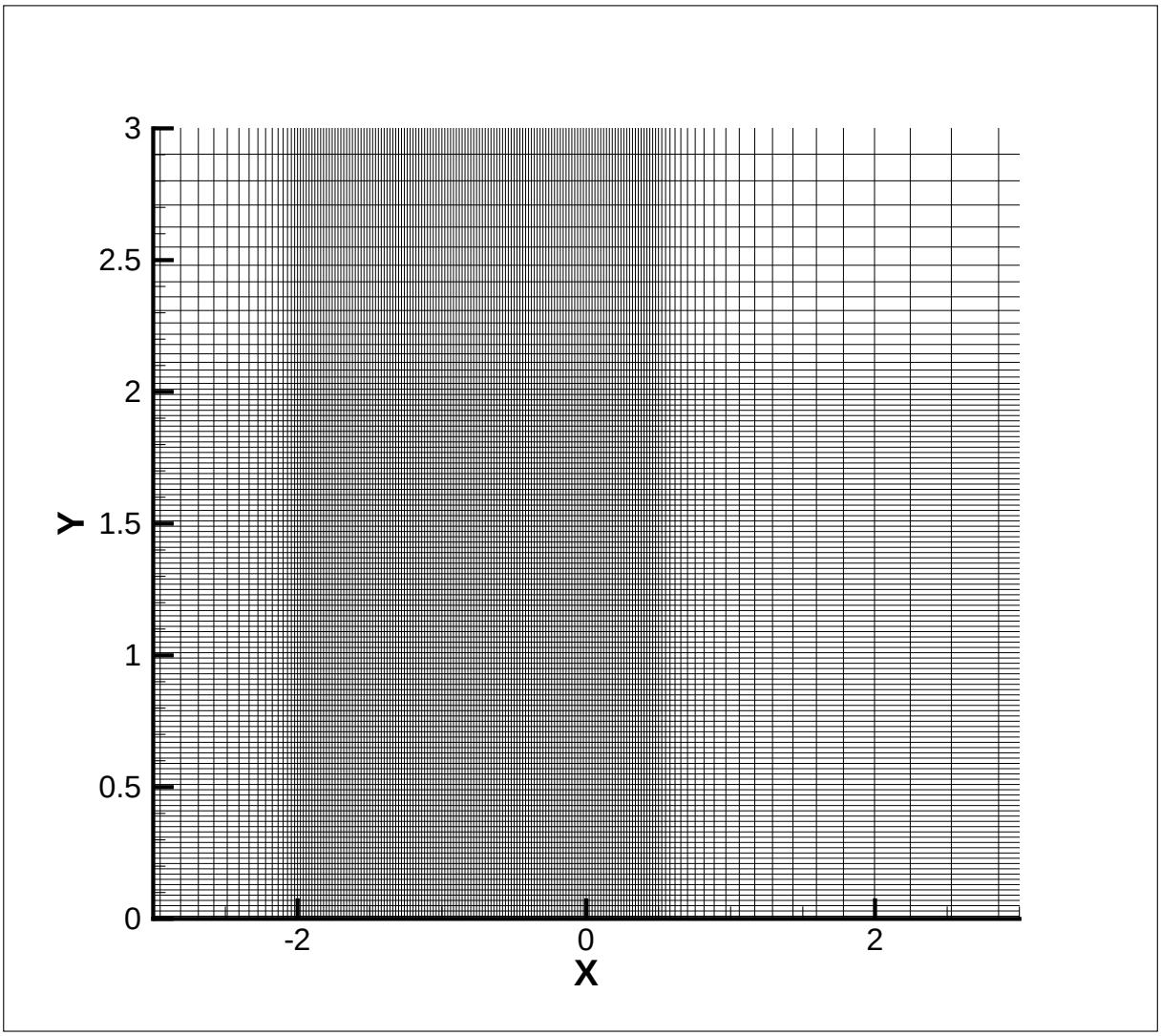

Figure 7.1: Mesh with uniformity in $\hat{y}$ ending at $\hat{y} = 2$ in the vertical direction and with uniformity ending at $\bar{x} = -2$ and $\bar{x} = \frac{1}{2}$ in the horizontal direction.

Chapter 8

Validation

As a check on our scheme, several validation tests were performed. The simplest validation was done by setting $K_1 = 1, K_{\frac{3}{2}} = 0, K_2 = 0, K_3 = 0$ and $\nu = 0$ in (7.1) to recover Laplace's equation. The wing shape used for this validation was the circular arc with the function f for the circular arc was written as

$$f = 1 - 4\bar{x}^2 \quad for \quad -\frac{1}{2} \leq \bar{x} \leq -\frac{1}{2},$$

Numerical results were compared to the exact solution, which was derived through the use of superimposed sources and sinks along the wing. The results matched well, meaning the general approach and differencing was working well. The solution was calculated using 50-200 points on the wing with the grid stretching factor of 15%. The solution at $\hat{y} = 0$ (on the wing) compared to exact solution can be seen in Figure 8.1 and a $\bar{x} = 0$ cut compared to exact solution can be seen in Figure 8.2. As one can see, the curves with different amount of points on the wing are almost indistinguishable. If one is to magnify Figure 8.1 to see the differences between the curves more closely, it can be seen that although the scheme is of second order in grid size, it behaves like a first order scheme because of the discontinuities at the leading and trailing edge of the wing.

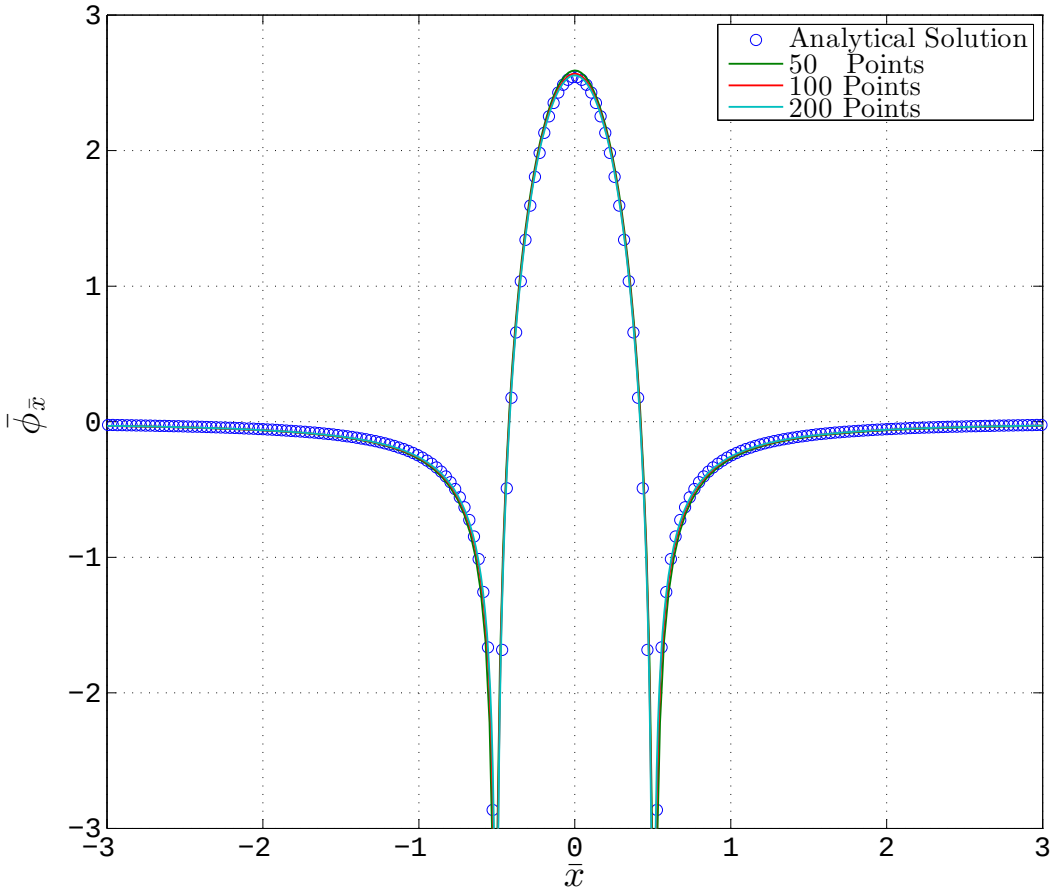

Figure 8.1: Comparison of the numerical solution with increasing amount of points on a circular arc wing compared to exact analytical solution at $\hat{y} = 0$.

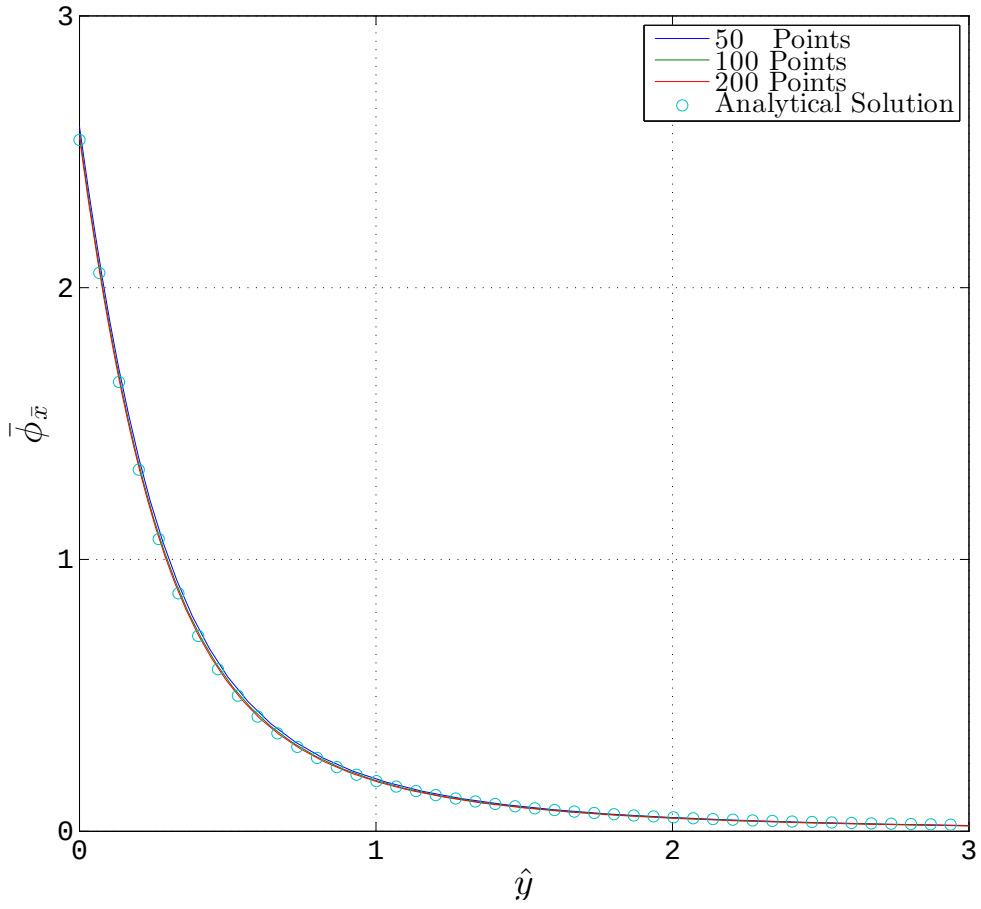

Figure 8.2: Comparison of the numerical solution with increasing amount of points on a circular arc wing compared to exact analytical solution at $\bar{x} = 0$.

The NACA 00XX boundary condition was implemented by using the wing shape equation, f, found in [8]. We modified the equation given by [8] slightly to close the trailing edge while retaining a maximum value of f of 1. We also shifted the wing to span $-\frac{1}{2} \leq \bar{x} \leq \frac{1}{2}$. This was done by changing the last coefficient in the equation to -0.1036, by dividing the whole equation by 1.000103738292760, and by adding $\frac{1}{2}$ to each $\bar{x}$. A factor β was placed in front of the equation. This allowed for an easy way to change the thickness of the wing.

$$y = \frac{10\beta}{1.000103738292760}[0.2969\sqrt{\bar{x}+0.5} - 0.1260(\bar{x}+0.5) \\ -0.3516(\bar{x}+0.5)^2 + 0.2843(\bar{x}+0.5)^3 - 0.1036(\bar{x}+0.5)^4] \tag{8.1}$$

By setting K_1 to some value and setting $K_{\frac{3}{2}} = 2, K_2 = 0, K_3 = 0$, we recover the classical transonic small disturbance equation. Since the analytical solution to the classical transonic

small disturbance equation has not yet been developed, we have checked the dependence of the solution on the number of grid points. This can be see in Figure 8.3, where the classical transonic equation was calculated over the NACA 00XX wing. It should be noted that the discrepancy in the solutions with different resolution is greater in the transonic small disturbance case. This can be attributed to the singularity at the normal shock. This singularity is known as the Zierep Singularity, which was described in detail in [22]. It was also tested that the shock jump condition was being satisfied for a classical transonic flow over the NACA 00XX. From the normal shock jump condition for the classical transonic small disturbance equation, we have

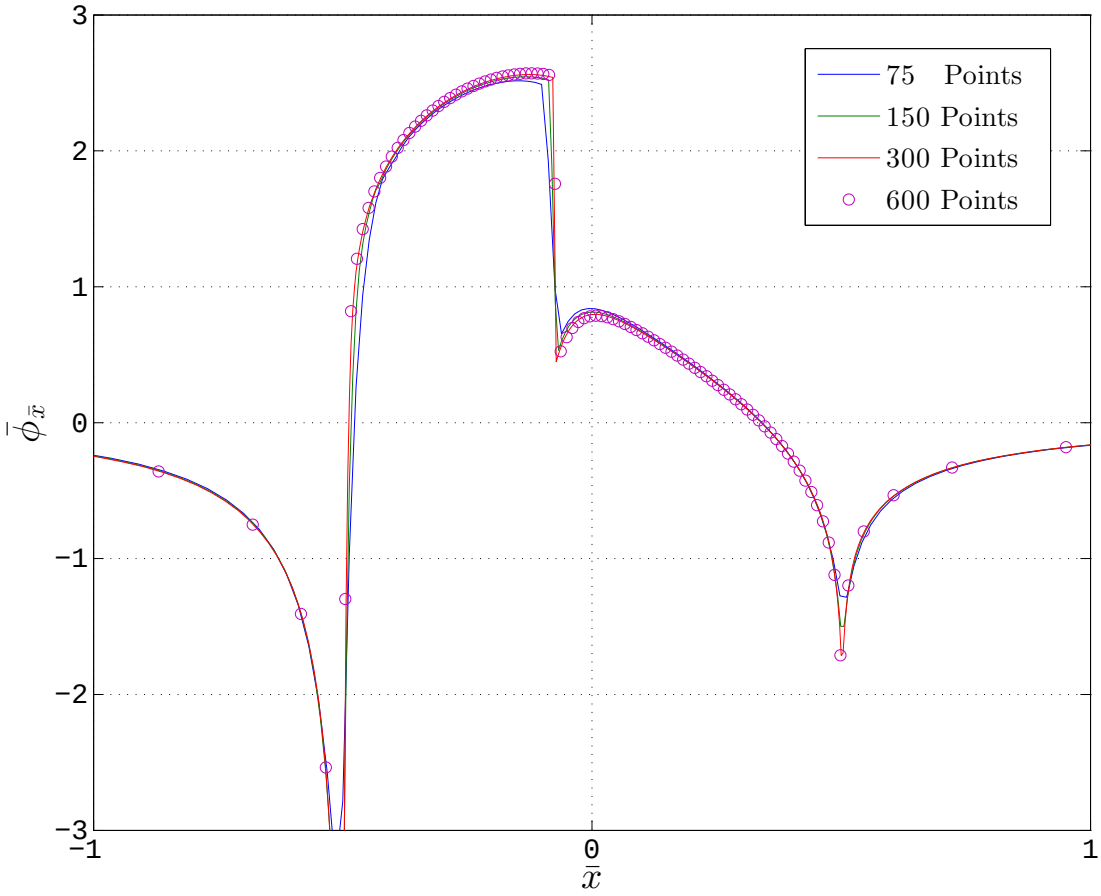

Figure 8.3: Grid convergence test of the numerical solution on the NACA 00XX wing ($\hat{y} = 0$) of the classic transonic small disturbance equations with increasing amount of grid points.

$$K_1 = \bar{\phi}_{\bar{x}}^{(2)} + \bar{\phi}_{\bar{x}}^{(1)}, \tag{8.2}$$

for which the derivation can be seen in [1]. In (8.2), the superscripts (1) and (2) indicate the value of $\bar{\phi}_{\bar{x}}$ upstream and downstream of the shock respectively. In this particular case, the parameters were set as $K_1 = 2.9, K_{\frac{3}{2}} = 2, K_2 = 0, K_3 = 0$ which resulted in a normal compression shock wave on the wing. Table 8.1 shows the percent error in (8.2) compared to the exact K_1. The error percentage decreases with the increase of the number of points on the wing as expected. The errors are quite large even though the resolutions are high. This is attributed to the difficulty in resolving the Zierep Singularity at the normal shock.

Table 8.1: $K_1 = 2.9$ Compared to Calculated K_1 for Different Resolutions

Number of Points on the Wing	Calculated K_1	% Error
75	3.14	8.28
150	3.06	5.52
300	2.99	3.10
600	2.95	1.72

For both supersonic and subsonic free streams, boundary interactions were a concern. It was determined that the boundaries at $\bar{x}_{min} = -6, \bar{x}_{max} = 6$, and $\hat{y} = 7$ were only sufficiently far away as long as there was no interaction between shocks several chord lengths away from the wing, or if the shocks and disturbance died out very quickly as in classical transonic flow cases. For most cases, the boundaries were extended to 40 chord lengths away in both the $\bar{x}$ and $\hat{y}$ directions. Because of the grid stretching, this increase did not add a significant increase in computation time. For the supersonic cases, boundary interaction was a major concern. With boundaries extending sufficiently far away, the solution close to the wing was effected minimally. The biggest discrepancy lies in the shock waves off the wing, which sometimes slightly moved with the change of boundary distance. An example of a rather complex subsonic solution with $M_\infty \approx 1$ with different far field boundaries can be seen in Figure 8.4. A similar test with a supersonic case can be seen in Figure 8.5.

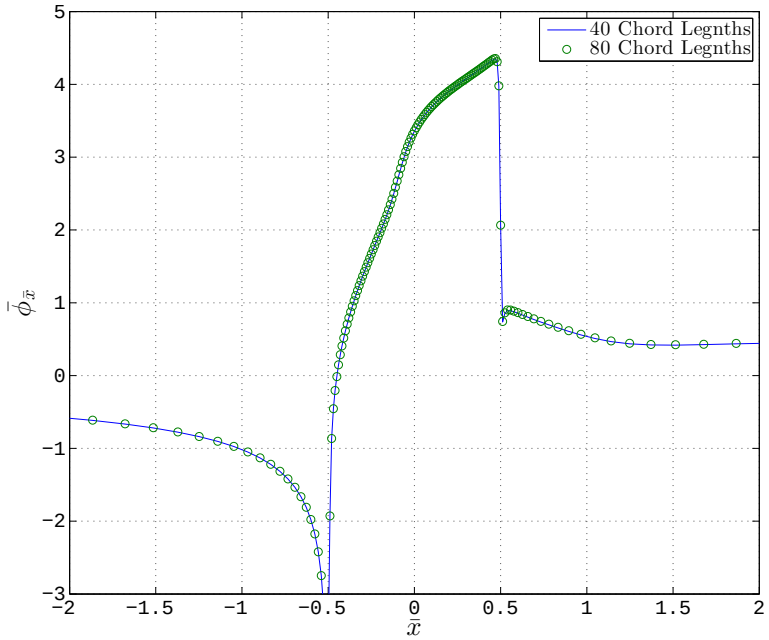

Figure 8.4: Numerical solution of the non-classical transonic small disturbance equations on the NACA 00XX wing ($\hat{y} = 0$) with increasing boundary distance, with a subsonic free stream, and with $M_\infty \approx 1$, $K_1 = 0.05, K_2 = 1.35, K_3 = 0.69$.

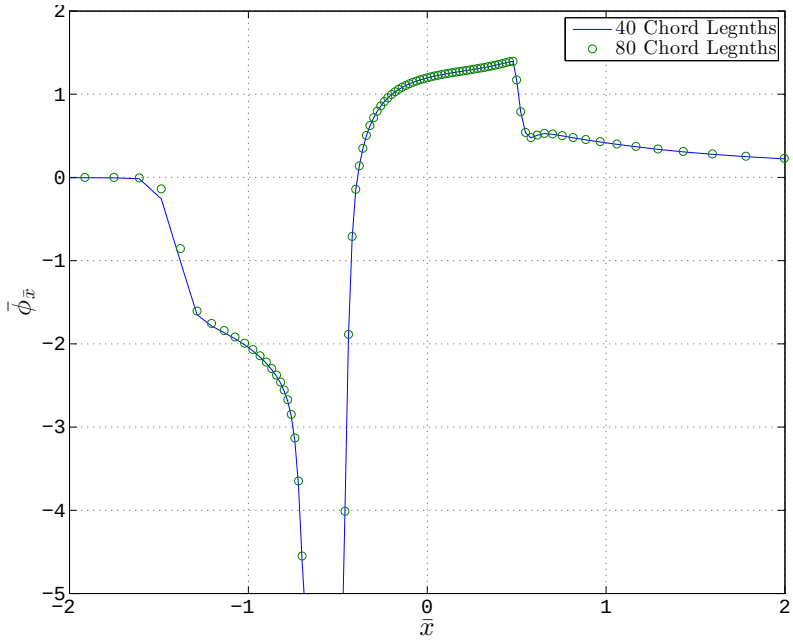

Figure 8.5: Numerical solution of the non-classical transonic small disturbance equations on the NACA 00XX wing ($\hat{y} = 0$) with increasing boundary distance, with a supersonic free stream, and with $M_\infty \approx 1$, $K_1 = -1, K_2 = -0.9, K_3 = 0.34$.

Chapter 9

Results

9.0.1 Case 1: Subsonic Free Stream Flow With $K_2 > 0$ and $K_3 > 0$

The first case we consider is a subsonic flow over a NACA 00XX wing with a free stream state near a high pressure zero of $\tilde{\Gamma}_\infty$. The value of Λ_∞ is therefore > 0 and we will also choose $\tilde{\Gamma}_\infty > 0$ such that $K_2 > 0$ and $K_3 > 0$. For this case we choose $K_2 = 1.35$ and $K_3 = 0.69$. The variation of the flux function (5.15) with $\hat{\rho}$ is plotted in Figure 9.1 for $K_1 = 0.05, 0.60, 1.00$. We first consider the flow corresponding to $K_1 = 1.00$, which, when the free stream thermodynamic state is fixed and ϵ and β are fixed, corresponds to the lowest free stream Mach number. Inspection of the $K_1 = 1.00$ curve in Figure 9.1 reveals that there is only one sonic point at $\hat{\rho} \approx -4$ on the insentrope, but because of the region of downward curvature, it passes through the region of $\tilde{\Gamma}_{local} < 0$. For the first computation we take β in (8.1) to be 1 and have plotted the computed variation of $-\hat{\rho}$ on the wing in Figure 9.2. A contour plot of $-\hat{\rho}$ is given in Figure 9.3 and the variation of the local Mach number on the wing is given in Figure 9.4. The minimum value of $\hat{\rho}$ is found to be about -3.75 and the flow is therefore entirely subsonic on the wing, which can also be seen by an inspection of Figure 9.4. Thus, the large gradients in $\hat{\rho}$ seen in Figures 9.2 and 9.3 do not correspond to shocks. Rather, the gradients are a rapid but isentropic expansion and compression. The left most local maximum and minimum of M in Figure 9.4 correspond to the inflection points seen in Figure 9.4. The central local maximum in M corresponds to the local maximum in $-\hat{\rho}$ in Figure 9.2. Because the Mach number tends to achieve a local maximum at subsonic values, cases of this type are often associated with flows having very large critical Mach numbers; see [3].

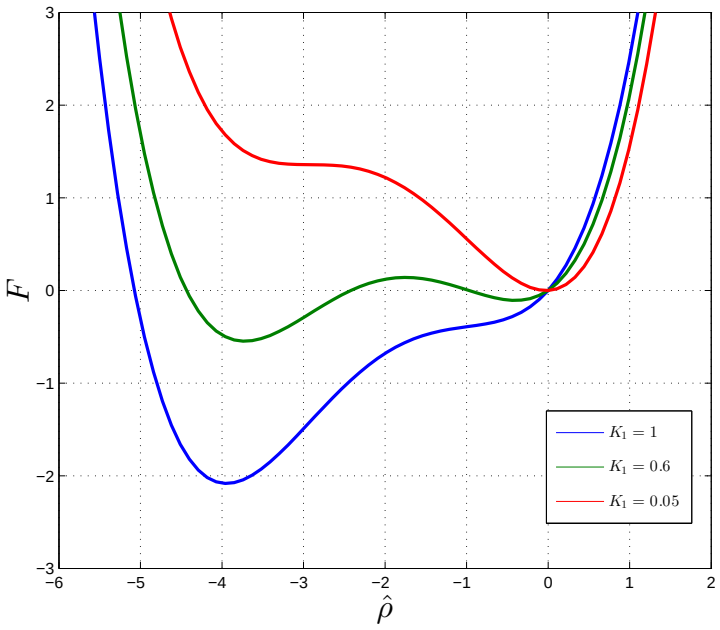

Figure 9.1: F curves for the first case with varying K_1 and $K_2 = 1.35, K_3 = 0.69$.

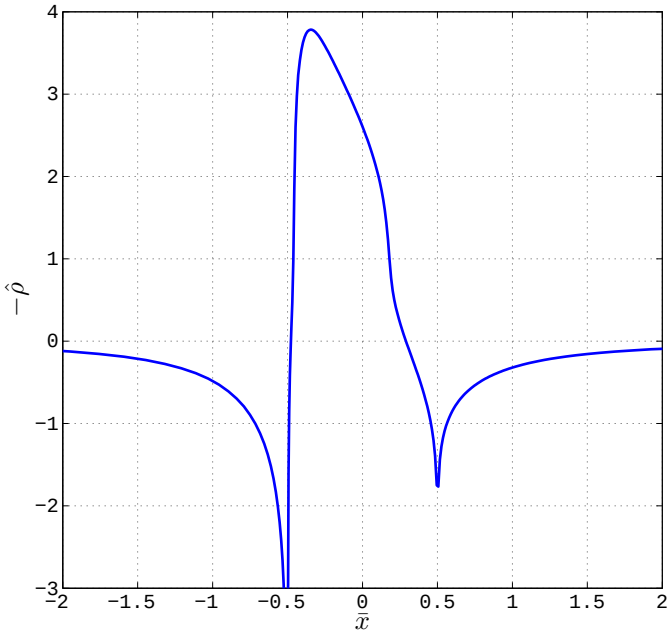

Figure 9.2: Density distribution of a subsonic free stream flow with $\beta = 1$ and $K_1 = 1, K_2 = 1.35$, and $K_3 = 0.69$.

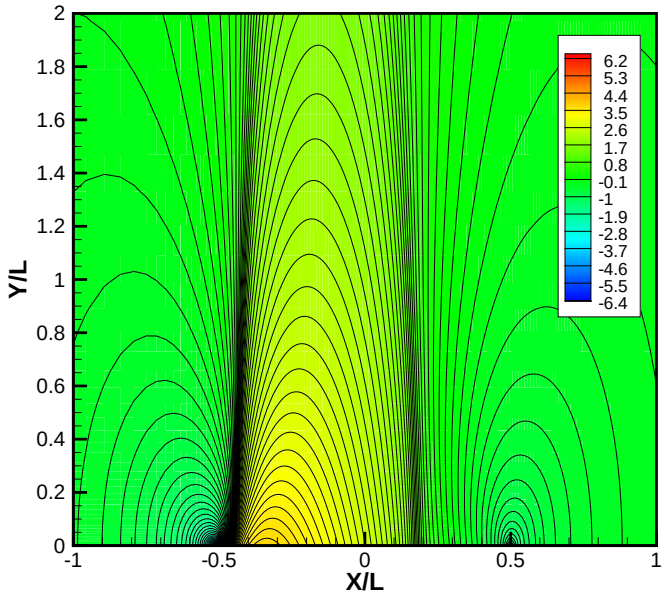

Figure 9.3: Contour plot of the density distribution of a subsonic free stream flow with $\beta = 1$ and $K_1 = 1, K_2 = 1.35$, and $K_3 = 0.69$. Contour steps of $\Delta\hat{\rho} = 0.1$

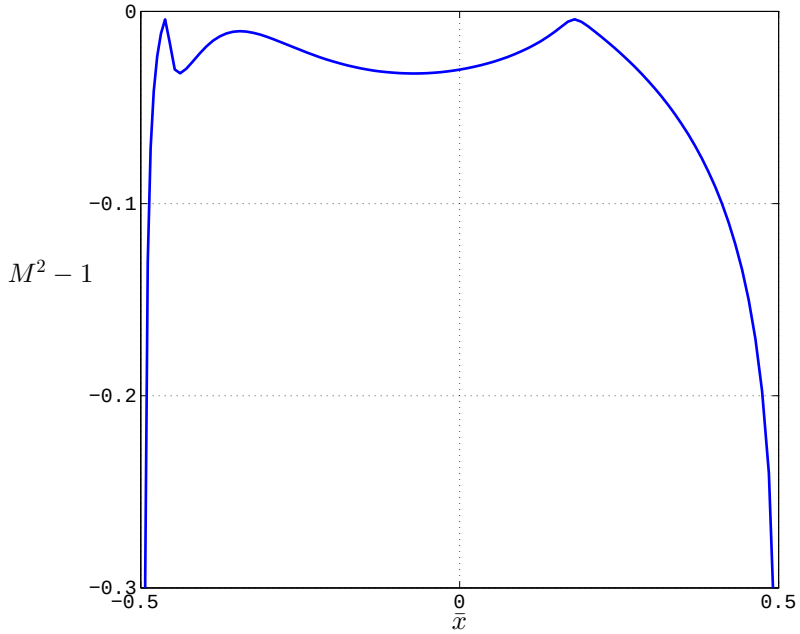

Figure 9.4: Mach number distribution of a subsonic free stream flow with $\beta = 1$ and $K_1 = 1, K_2 = 1.35$, and $K_3 = 0.69$

The next flow considered corresponds to a thicker airfoil having $\beta = 1.3$ in (8.1). In this case, the expansion over the wing is stronger and the flow becomes supersonic near the minimum pressure. The re-compression of the flow as it approaches the trailing edge causes a conventional compression shock to form. The $\hat{\rho}$ and Mach number distribution on the wing and the corresponding contour plot is provided in Figures 9.5-9.7.

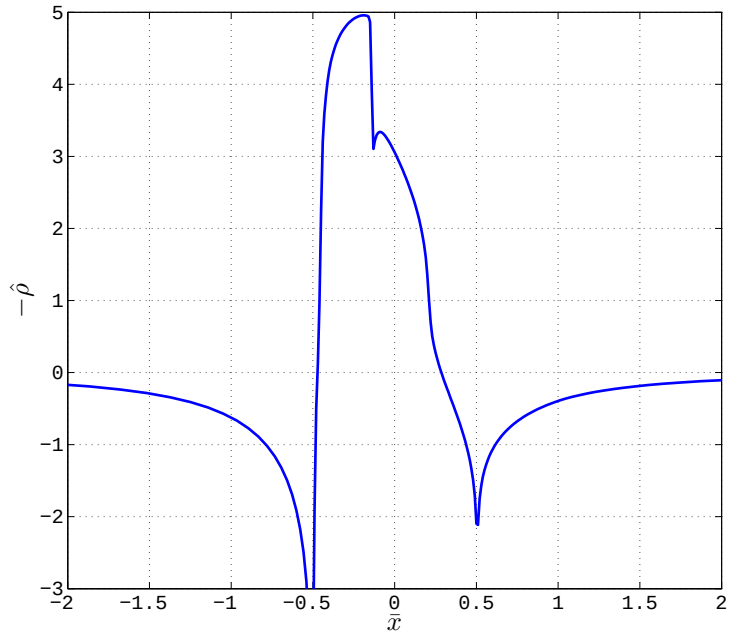

Figure 9.5: Density distribution of a subsonic free stream flow with $\beta = 1.3$ and $K_1 = 1, K_2 = 1.35$, and $K_3 = 0.69$

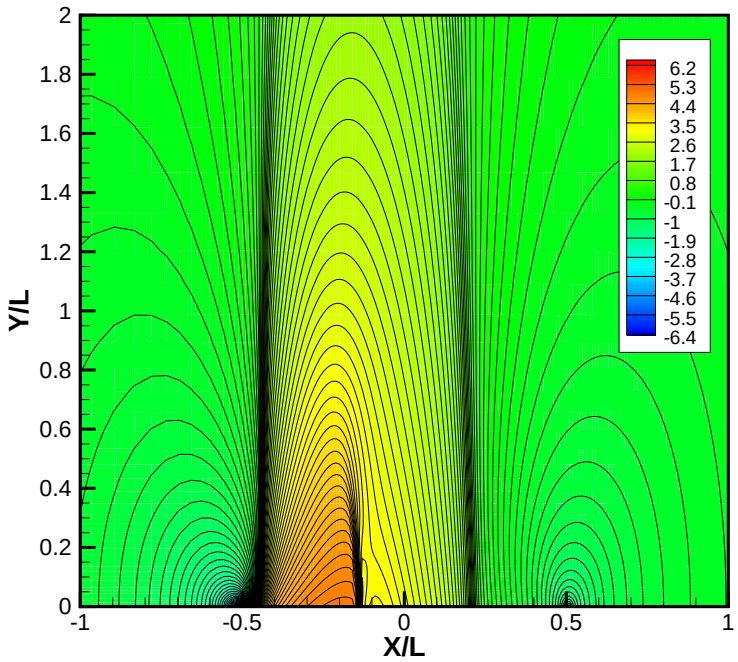

Figure 9.6: Contour plot of the density distribution of a subsonic free stream flow with $\beta = 1.3$ and $K_1 = 1, K_2 = 1.35$, and $K_3 = 0.69$. Contour steps of $\Delta\hat{\rho} = 0.1$

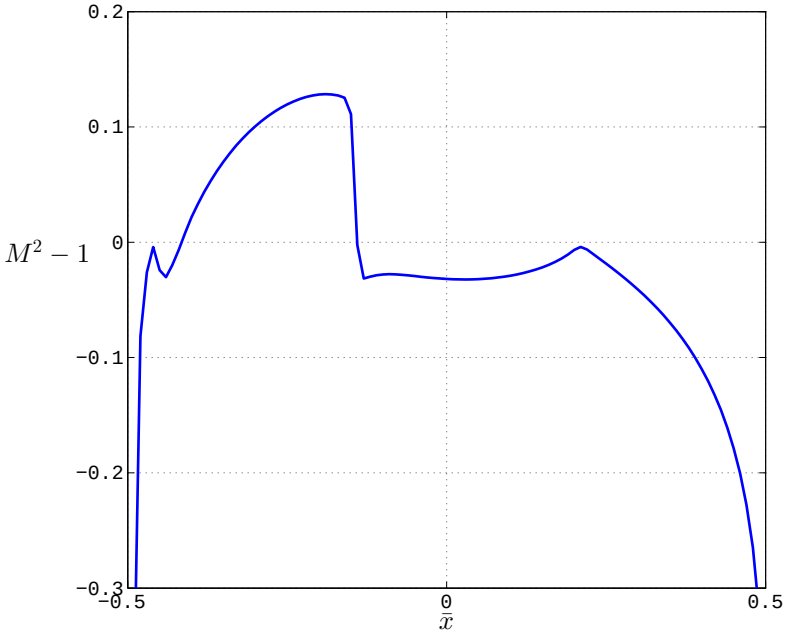

Figure 9.7: Mach number distribution of a subsonic free stream flow with $\beta = 1.3$ and $K_1 = 1, K_2 = 1.35$, and $K_3 = 0.69$

In the next case to be considered, we reduce K_1 to 0.6, which corresponds to a higher Mach number if all of the thermodynamic free stream conditions are kept the same as in the previous cases. The F curve now has a local maximum and two local minimums resulting in a total of three sonic points on the free stream isentrope. We begin by considering a relatively small value of $\beta = 0.5$. The variation of F with $\hat{\rho}$, the computed variation of $-\hat{\rho}$ on the wing, and the corresponding contour plot are provided in Figures 9.8 - 9.10. This indicates that expansion shocks and sonic shocks can now be present in the flow. After emerging from the leading edge stagnation point, the flow becomes sonic at the point 1 labeled in Figure 9.8. According to the existence conditions stated in chapter 6, a variety of expansion shocks can form. However, on the wing, the only shocks that can form are normal shocks. One such normal expansion shock is sketched in Figure 9.8 as the horizontal line ($[\![F]\!] = 0$) $1 \rightarrow 2$. This expansion shock is clearly visible in Figure 9.10, but more difficult to identify in Figure 9.9. As the flow re-compresses to the stagnation point of the trailing edge, a normal sonic compression shock (represented by the Rayleigh line $3 \rightarrow 4$ in 9.10) forms. The flow then compresses from point 4 to the trailing stagnation point.

A comparison of Figure 9.9 - 9.10 reveals a difficulty in comparing points on a $-\hat{\rho}$ vs. $\bar{x}$ plot with those on a F vs. $\hat{\rho}$ plot. The combination of the numerical resolution of the Zierep singularity, the rapid variation at the leading and sometimes trailing edges, the large values of F' in some regions of the F vs. $\hat{\rho}$ curve, and numerical oscillations make precise comparisons difficult. Better quantitative results can sometimes be achieved by increasing the artificial viscosity ν. Nevertheless, many flows can be either predicted or explained in a qualitative manner by inspection of the F vs. $\hat{\rho}$ curve.

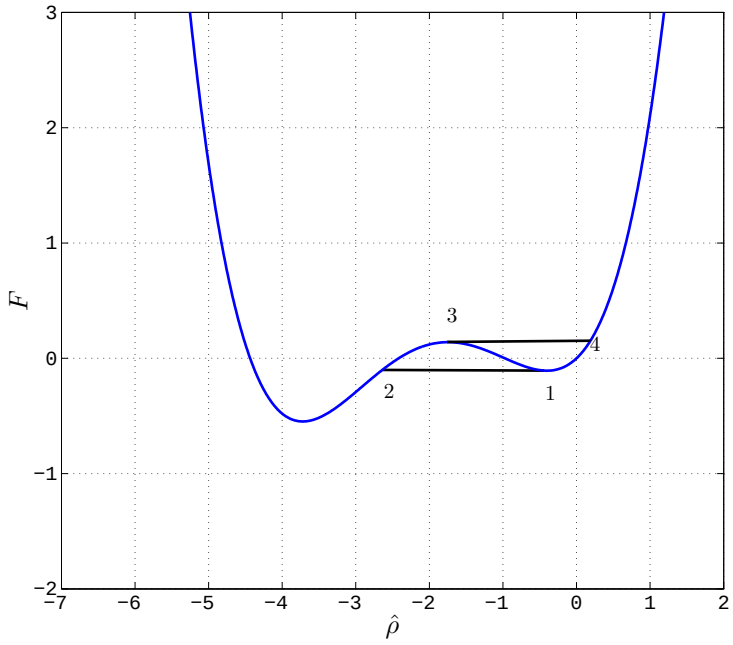

Figure 9.8: Rayleigh lines describing the strength and the type of shock waves present in the flow for the case with $\beta = 0.5$ and $K_1 = 0.6, K_2 = 1.35$, and $K_3 = 0.69$.

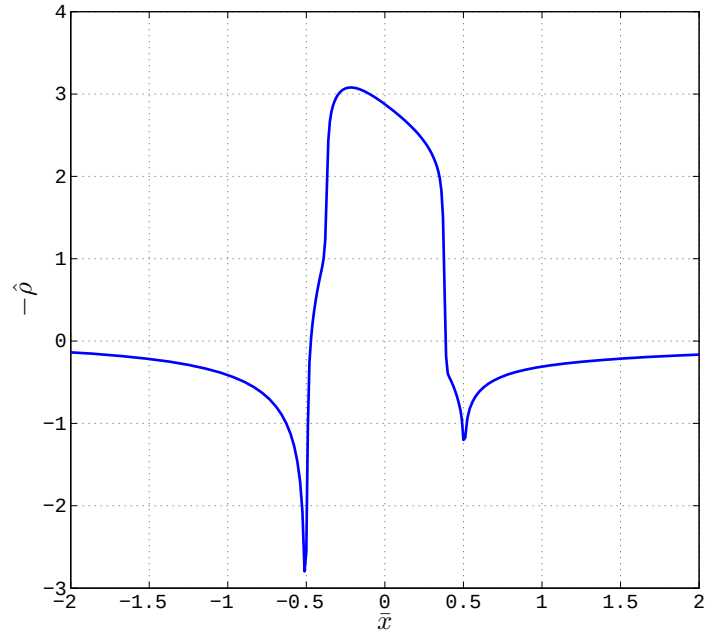

Figure 9.9: Density distribution of a subsonic free stream flow with $\beta = 0.5$ and $K_1 = 0.6, K_2 = 1.35$, and $K_3 = 0.69$.

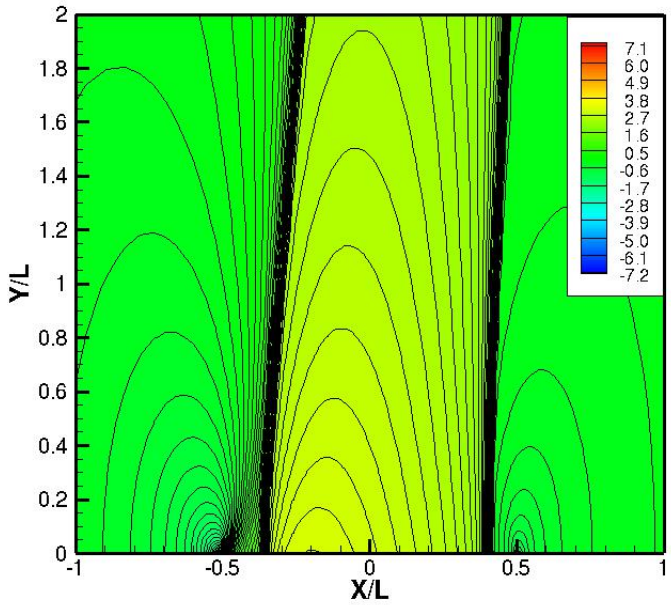

Figure 9.10: Contour plot of the density distribution of a subsonic free stream flow with $\beta = 0.5$ and $K_1 = 0.6, K_2 = 1.35$, and $K_3 = 0.69$. Contour steps of $\Delta\hat{\rho} = 0.1$

If we increase the wing thickness by increasing β to 0.7, this results in the flow passing the second local minimum point in the F curve, which permits two compression shocks to exist. Figure 9.11 shows the Rayleigh lines corresponding to the three shocks on the wing. The flow is therefore expected to expand from the leading edge stagnation point to the sonic point 1. A normal sonic expansion shock takes the flow from $1 \rightarrow 4$ followed by an isentropic expansion to the supersonic point 3. If $F_3 < F_5$, the compression will be accomplished through a normal shock from $3 \rightarrow 4$. The flow compresses from $4 \rightarrow 5$ isentropically. Depending on the trailing edge angle, the compression may occur through a normal shock, e.g., the shock represented by $5 \rightarrow 6$, followed by an isentropic compression to stagnation. For the chosen β, this flow pattern was observed and has been plotted in Figures 9.12 - 9.13.

The behavior of the three shocks far from the wing can be deduced by examining the F vs. $\hat{\rho}$ curve in Figure 9.11. For $y > 0$, the normal shocks become oblique shocks satisfying (6.7). The shock represented by $3 \rightarrow 4$ in Figure 9.11 will simply decay as both points 3 and 4 approach the sonic point at $\hat{\rho} \approx -3.7$. This is completely analogous to the behavior of the classical compression shock of transonic flow. Because each shock must satisfy (6.7), the shock represented by $3 \rightarrow 4$ will never collide with those represented by $1 \rightarrow 2$ and $5 \rightarrow 6$. However, it is possible that the downstream state of the expansion can equal the upstream state of the compression shock represented by $5 \rightarrow 6$. If the collision occurs, the result is expected to be a single oblique compression shock.

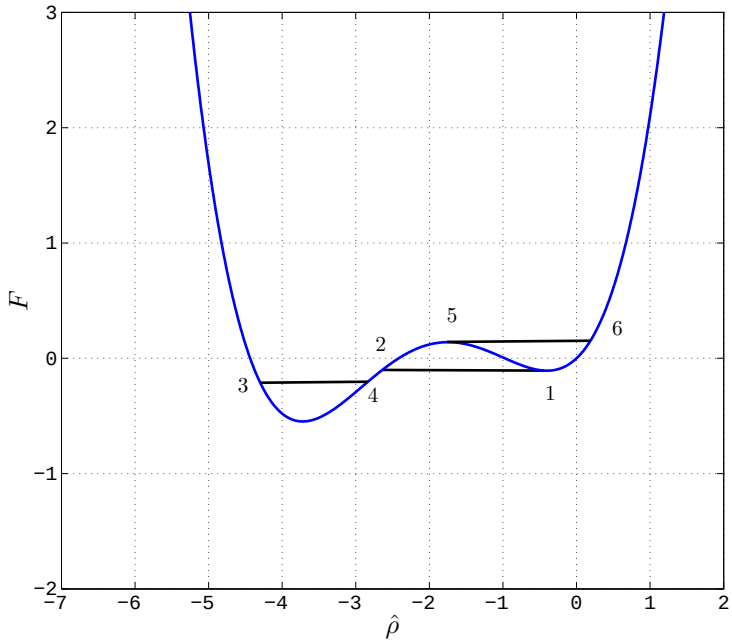

Figure 9.11: Rayleigh lines describing the strength and the type of shock waves present in the flow for the case with $\beta = 0.7$ and$K_1 = 0.6, K_2 = 1.35$, and $K_3 = 0.69$.

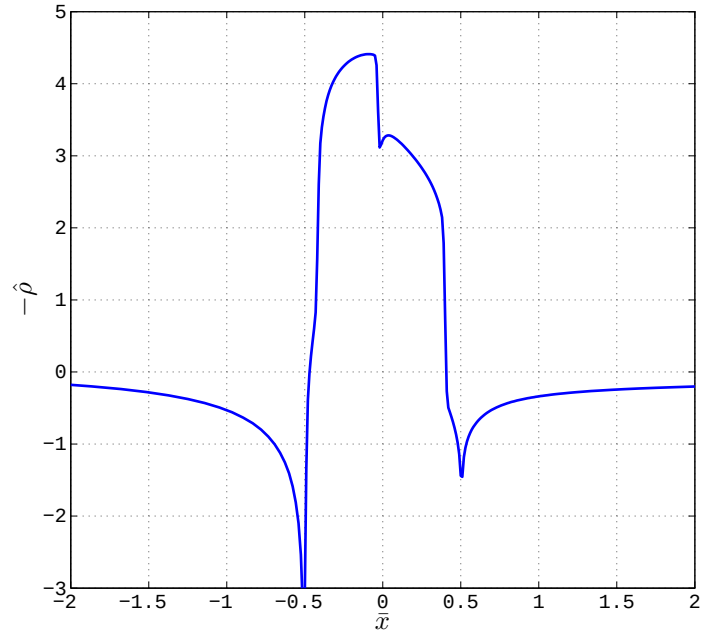

Figure 9.12: Density distribution of a subsonic free stream flow with $\beta = 0.7$ and $K_1 = 0.6, K_2 = 1.35$, and $K_3 = 0.69$.

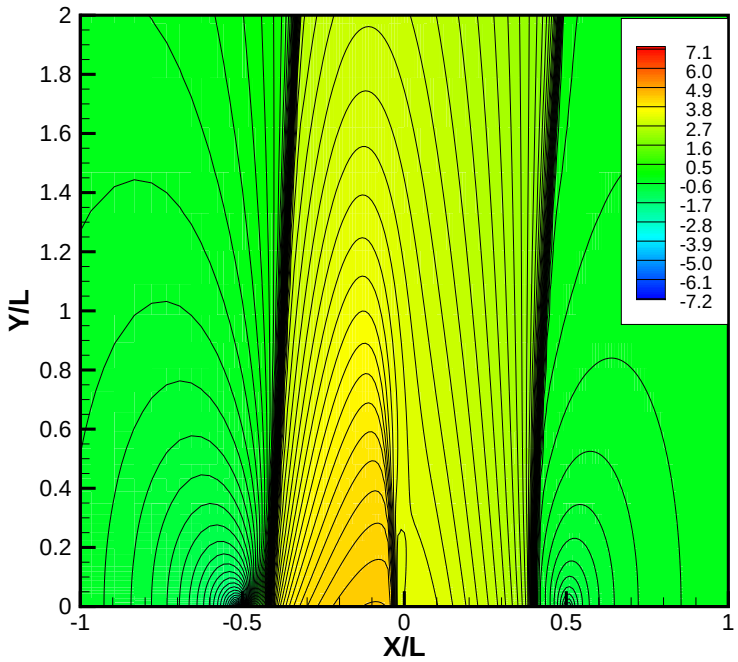

Figure 9.13: Contour plot of the density distribution of a subsonic free stream flow with $\beta = 0.7$ and $K_1 = 0.6, K_2 = 1.35$, and $K_3 = 0.69$. Contour steps of $\Delta\hat{\rho} = 0.1$

After making $\beta = 1.1$, we find that the flow profile changed to a split-shock configuration. As depicted in Figure 9.14, the minimum value of $\hat{\rho}$ is such that the compression from the minimum pressure can be accomplished through a single normal compression shock represented by shock $3 \rightarrow 4$ sketched in Figure 9.14. As this compression shock decays and becomes oblique, it ultimately becomes inadmissible and splits into two shocks separated by an isentropic compression; see, e.g., the discussion of shock splitting in Chapter 6. The variation of $-\hat{\rho}$ on the wing and contour plot are provided in Figures 9.15 - 9.16. One way to view the transition from the $\beta = 0.7$ case to the $\beta = 1.1$ case is that the two compression shocks in the first case have collided, forming the merged shock of the case $\beta = 1.1$. Alternatively, we may regard the split point as having moved from a $y > 0$ point to the wing at some $0.7 < \beta < 1.1$.

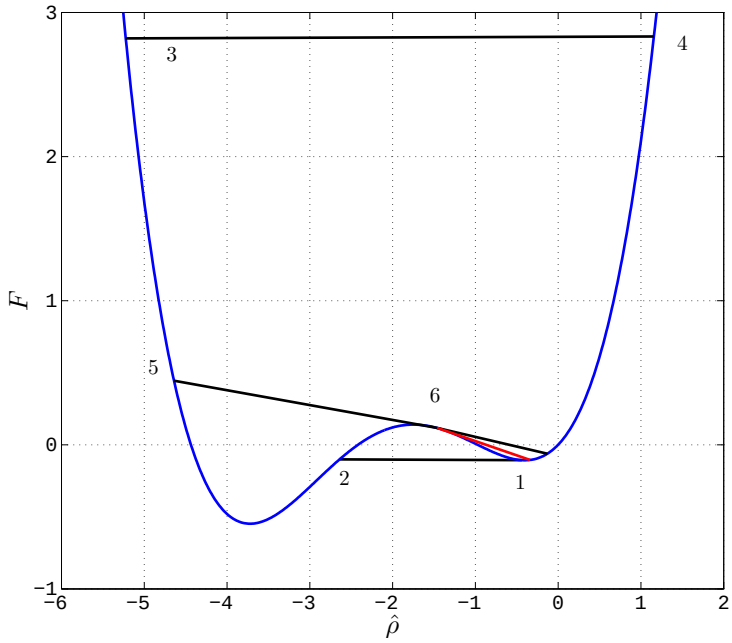

Figure 9.14: Rayleigh lines describing the strength and the type of shock waves present in the flow for the case with $\beta = 1.1$ and $K_1 = 0.6, K_2 = 1.35$, and $K_3 = 0.69$. The split shock is indicated in red.

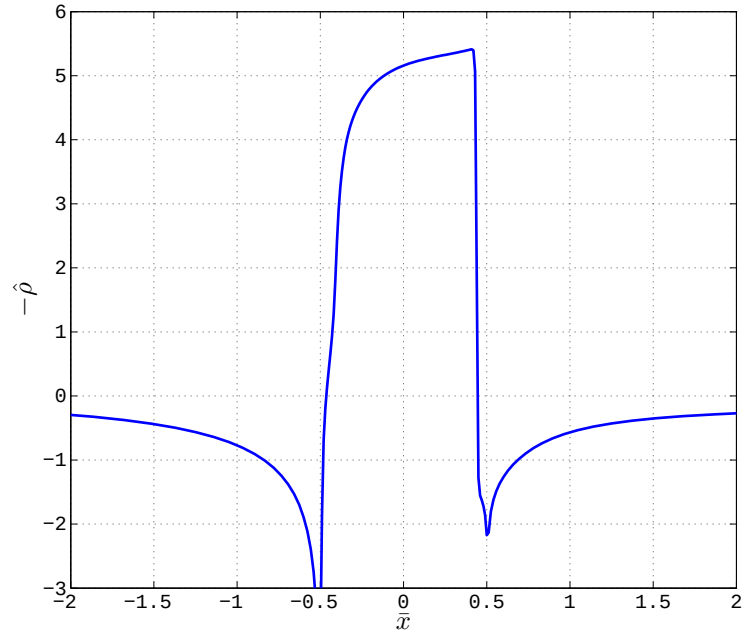

Figure 9.15: Density distribution of a subsonic free stream flow with $\beta = 1.1$ and $K_1 = 0.6, K_2 = 1.35$, and $K_3 = 0.69$.

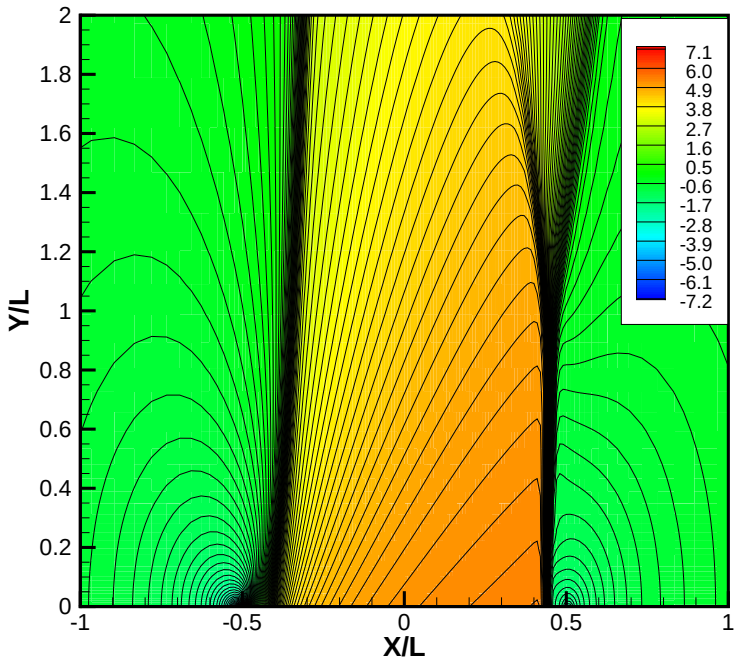

Figure 9.16: Contour plot of the density distribution of a subsonic free stream flow with $\beta = 1.1$ and $K_1 = 0.6, K_2 = 1.35$, and $K_3 = 0.69$. Contour steps of $\Delta\hat{\rho} = 0.1$

Changing β to a final and even larger value, $\beta = 2$, changes the behavior of the flow once again. Now the value of β is large enough to accelerate the flow enough to convert the normal shock on the wing to the trailing edge oblique shock. Also the presence of a stern shock is now apparent in Figures 9.18 and 9.19. A schematic of the shocks is provided in Figure 9.17. The expansion shock remains unchanged. The oblique shock is represented by the Rayleigh line $3 \rightarrow 4$. After the oblique shock the flow compresses isentropically from $4 \rightarrow 5$ until a normal compression shock ($5 \rightarrow 6$) is formed; this is the stern shock seen $\bar{x} \approx 0.75$ in Figures 9.18 - 9.19. As y increases, the disturbance progressively weakens. The red line represents the point in the flow above the wing where the downstream conditions of the oblique shock are equal to the upstream conditions to the normal stern shock. The collision between the two shock waves produces a new oblique shock, shown in green. The green line has the same fate as the split shock in the $\beta = 1.1$ case. The produced shock wave splits as can be seen in Figure 9.19, near he local maximum of F seen in 9.17.

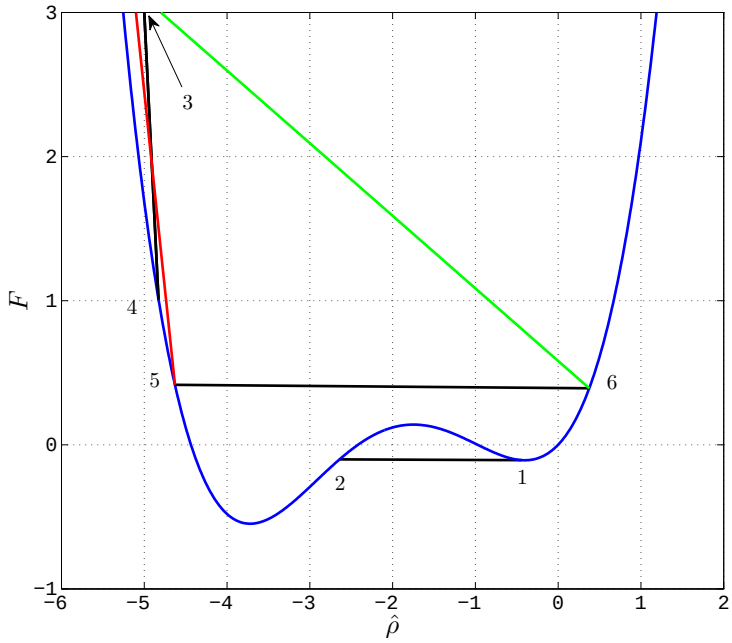

Figure 9.17: Rayleigh lines describing the strength and the type of shock waves present in the flow for the case with $\beta = 2$ and $K_1 = 0.6, K_2 = 1.35$, and $K_3 = 0.69$. The shock collision is indicated in red and the resultant shock is indicated in green.

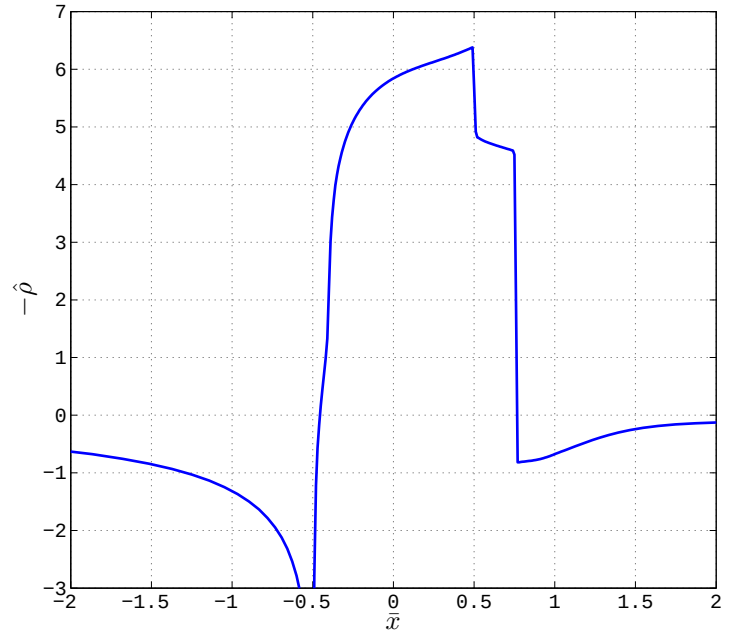

Figure 9.18: Density distribution of a subsonic free stream flow with $\beta = 2$ and $K_1 = 0.6, K_2 = 1.35$, and $K_3 = 0.69$.

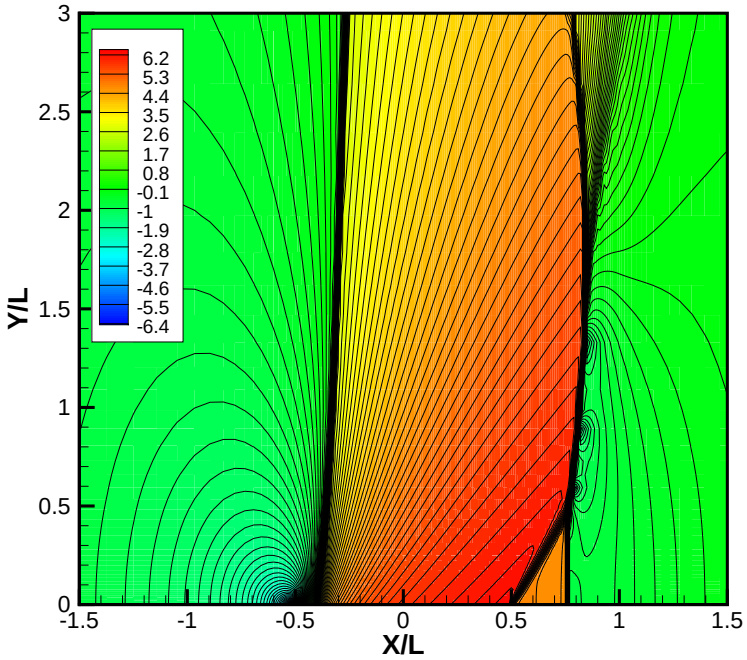

Figure 9.19: Contour plot of the density distribution of a subsonic free stream flow with $\beta = 2$ and $K_1 = 0.6, K_2 = 1.35$, and $K_3 = 0.69$. Contour steps of $\Delta\hat{\rho} = 0.1$

There is a value of $\beta \approx 1.3$ for this case of free stream parameters that seemingly produced two stern shocks, but theses shocks were extremely close to the trailing edge of the wing. Due to the singularity at the trailing edge of the wing, we could not resolve these shocks clearly and only the Mach number variation indicated their presence. A similar shock configuration is described more clearly in the next section.

We now reduce K_1 to represent an almost sonic free stream. We set $K_1 = 0.05$. The F vs. $\hat{\rho}$ plot is given in Figure 9.20. For this choice of parameters, there is only one sonic point and the region of $\tilde{\Gamma}_{local} < 0$ corresponds to $M > 1$. The only normal shocks which are possible are compression shocks. However, if the minimum value of $\hat{\rho}$ is to the left of at least the right most inflection point, an expansion shock might form in the $y > 0$ region. Points $1 \rightarrow 2$ indicate the possible expansion shocks that could form off the wing. The variation of $-\hat{\rho}$ vs. $\bar{x}$ and the contour plot for the case $\beta = 1$ is provided in Figures 9.21 and 9.22. In this case an oblique compression shock forms at the trailing edge, represented by the Rayleigh line $3 \rightarrow 4$ in Figure 9.20, and appears to quickly break into a shock fan combination. We note that examination of the Rayleigh line $3 \rightarrow 4$ in Figure 9.20 suggests that shock-splitting might be possible. However, there may be the aforementioned inaccuracies in the estimation of points $3 \rightarrow 4$ from Figure 9.21.

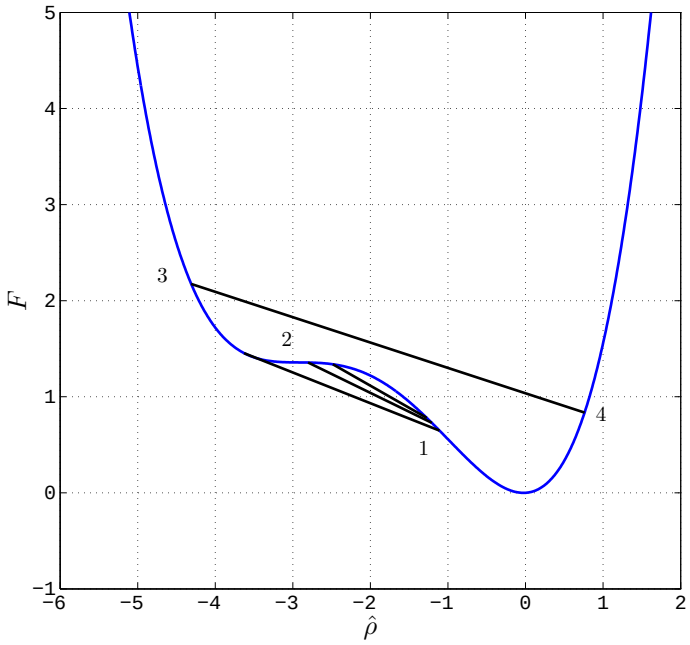

Figure 9.20: Rayleigh lines describing the strength and the type of shock waves present in the flow for the case with $\beta = 1$ and $K_1 = 0.05, K_2 = 1.35$, and $K_3 = 0.69$.

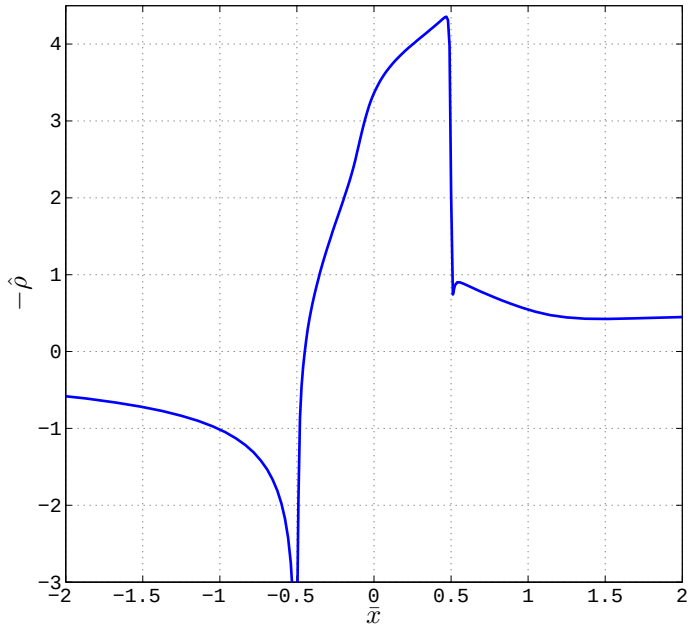

Figure 9.21: Density distribution of a subsonic free stream flow with $\beta = 1$ and $K_1 = 0.05, K_2 = 1.35$, and $K_3 = 0.69$.

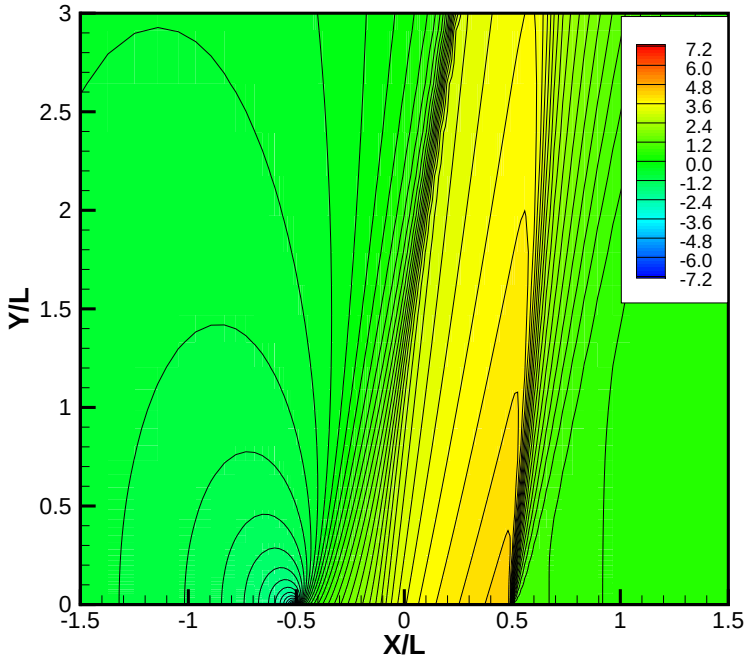

Figure 9.22: Contour plot of the density distribution of a subsonic free stream flow with $\beta = 1$ and $K_1 = 0.05, K_2 = 1.35$, and $K_3 = 0.69$. Contour steps of $\Delta\hat{\rho} = 0.2$

9.0.2 Case 2: Subsonic Free Stream Flow With $K_2 > 0$ and $K_3 < 0$

In this section we consider flows over the NACA00XX wing which are initiated at a free stream thermodynamic state such that $\Lambda_\infty < 0$ and $\tilde{\Gamma}_\infty < 0$. This is recognized as a state having pressures somewhat above the pressure corresponding to the low pressure or low density zero of $\tilde{\Gamma}$. The free stream Mach number will be taken to be less than unity so that the present case corresponds to $K_1, K_2 > 0, K_3 < 0$. The F vs. $\hat{\rho}$ variation for two values of K_1 are given in Figure 9.23. Inspection of (5.15) and (5.16) reveals that the F vs. $\hat{\rho}$ curves will be reflected about the F and $\hat{\rho}$ axes. It will therefore be convenient to use the plots of $-F$ vs. $-\hat{\rho}$ whenever $\tilde{\Gamma}_\infty < 0$. As in the case of $\tilde{\Gamma}_\infty > 0$, compressions correspond to motion to the right and expansions correspond to motion to the left.

We first consider the case corresponding to the lower free stream Mach number in Figure 9.23, i.e., $K_1 = 1.0$. The resultant F vs. $\hat{\rho}$ curve is seen to contain only one $M = 1$ point, i.e., only one $F' = 0$ point. Because of the similarity to the $K_1 = 1$ F curve seen in Figure 9.1, we expect that the present flow will be generally similar to that observed in the case associated with Figure 9.1. In order to illustrate the behavior for this case we have computed the flow from a NACA 00XX having $\beta = 0.7$ and plotted the results in Figures 9.24 - 9.26. For this wing thickness the flow is supercritical and a conventional normal compression shock is generated. Inspection of Figure 9.23 reveals that the Mach number will attain a

local maximum as the leading edge stagnation point is approached. This corresponds to the inflection point ($F'' = 0$) located at $-\hat{\rho} \approx 0.8$ in Figure 9.23. The same local maximum occurs after the trailing edge. The local maximum in M occurs at two points on the wing, but the local maximum near the leading edge is poorly resolved in Figure 9.24. As in the case associated with Figures 9.2 - 9.3, the local maxima are associated with a steepening of the pressure and density distribution. In the present case, this steepening occurs both before and after the leading edge and before and after the trailing edge.

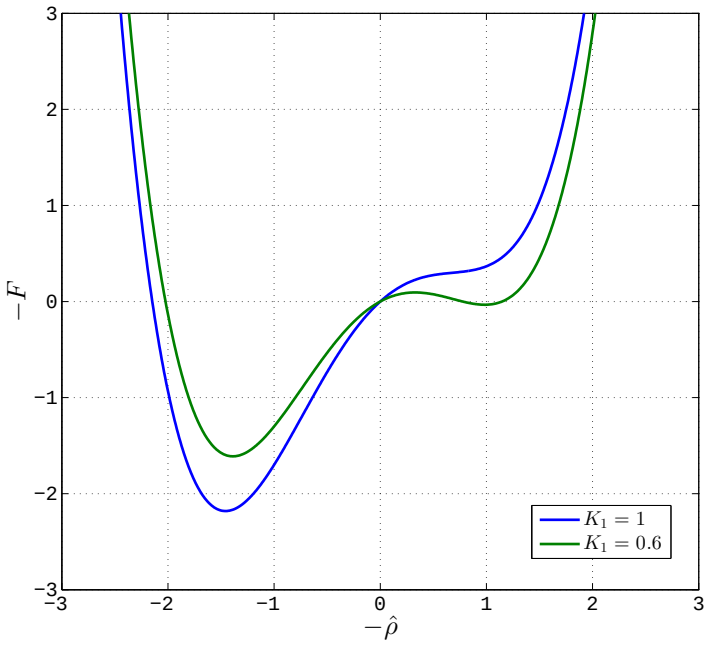

Figure 9.23: F curves for the second case with varying K_1 and $K_2 = 0.1, K_3 = -4$.

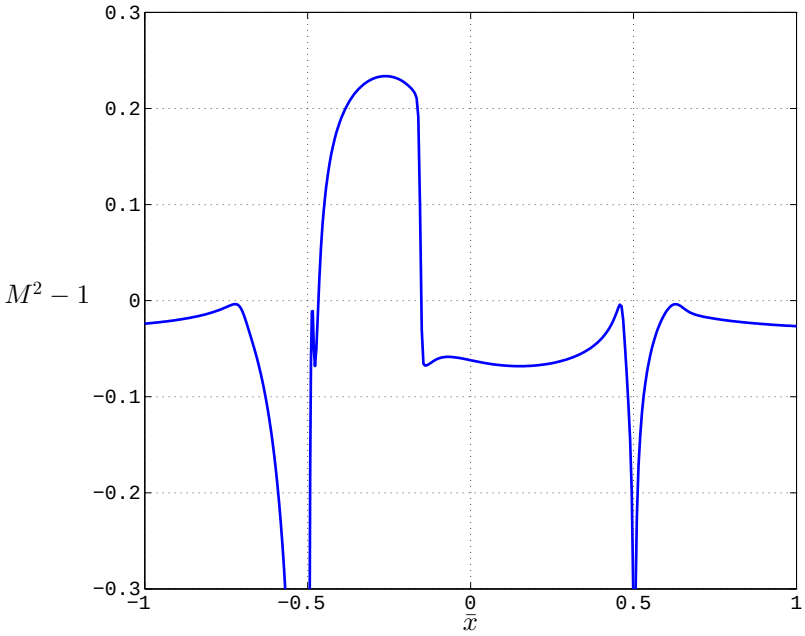

Figure 9.24: Mach number distribution of a subsonic free stream flow with $\beta = 0.7$ and $K_1 = 1, K_2 = 0.1$ and $K_3 = -4$.

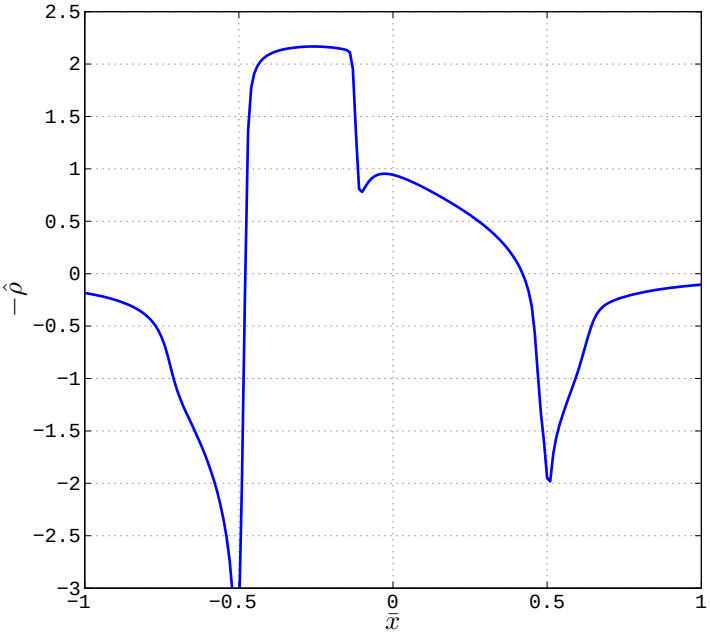

Figure 9.25: Density distribution of a subsonic free stream flow with $\beta = 0.7$ and $K_1 = 1, K_2 = 0.1$ and $K_3 = -4$.

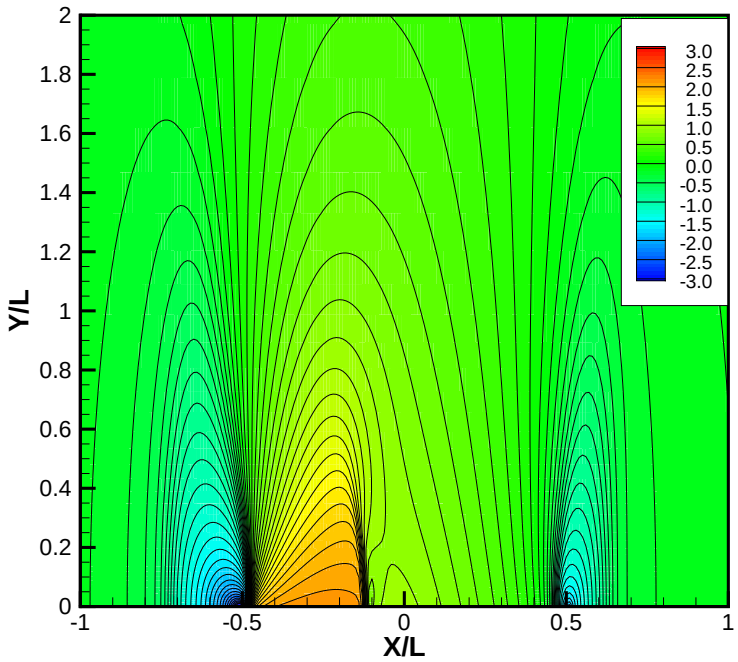

Figure 9.26: Contour plot of the density distribution of a subsonic free stream flow with $\beta = 0.7$ and $K_1 = 1, K_2 = 0.1$ and $K_3 = -4$. Contour steps of $\Delta\hat{\rho} = 0.1$

If we now increase the free stream Mach number such that $K_1 = 0.6$, there will be three sonic ($M = 1$) points along the F curve of Figure 9.27. The two new $M = 1$ points occur in the compressive portions of the flow, i.e., where $-\hat{\rho} > 0$. Thus, as the flow approaches the leading edge stagnation point ($-\hat{\rho} \to \infty$) from the free stream, the fluid must pass through a region of supersonic flow. As a result, a normal compression shock can, and typically does, form in front of the wing. The F curve, wing density distribution, and contour plot for this case is plotted in Figures 9.27 - 9.29. This bow compression shock is represented by the Rayleigh line $1 \to 2$ in Figure 9.27 and can be seen in the density distribution of Figure 9.28. It is important to note that this bow shock occurs when the free stream is subsonic ($K_1 > 0$) and is not due to conventional detachment. Rather, it is due to the non-monotone Mach number variation associated with the non-convex flux function. The occurrence of bow compressive shocks was first predicted and observed by [2] in the context of a $\Xi_\infty = 0$ theory.

A more complete description of the flow for this case can be obtained by following the flow as it passes over the wing. As the flow leaves the leading edge stagnation point, the sonic ($M_3 = 1$) point at 3 and a normal expansion shock can, and typically does, form on the wing. This normal shock is represented by the Rayleigh line $3 \to 4$. For this value of β, the minimum value of $-\hat{\rho}$ is approximately 1.25 and remains subsonic there. After the local minimum in $-\hat{\rho}$ is attained, the flow compresses as the trailing edge stagnation point ($-\hat{\rho} \to \infty$) is approached. The flow again becomes sonic ($M_5 = 1$) at point 5 resulting in a

normal compression shock from $5 \rightarrow 6$. As the flow leaves the stagnation point at the trailing edge it again becomes sonic ($M_7 = 1$) at point 7. A normal expansion shock, denoted by $7 \rightarrow 8$ in Figure 9.27, forms a stern shock in order to bring the flow back to the free stream conditions. The stern expansion shock is clearly evident in Figures 9.28 - 9.29. Inspection of Figure 9.28 also reveals that much of the compression required as the trailing edge is approached occurs smoothly over length scales on the order of the wing chord. This, along with similar observations, provides support for the idea that the natural dynamics of BZT fluids frequently can reduce adverse pressure gradients on conventional wing profiles.

As the normal shocks move away from the wing they become oblique. The Rayleigh lines associated with these shocks must have negative slopes in Figure 9.27. It can be verified by analysis of Figure 9.27 that collisions between expansion and compression shocks can only occur between shocks originating as $5 \rightarrow 6$ and $7 \rightarrow 8$. That is, the expansion and compression shock originating on the wing cannot collide with each other and the bow shock and stern shock cannot collide with each other. This differs from the cases depicted in the previous section where the undulations in F, leading to the possibility of sonic compression and expansion shocks, occurred in the expansive portion of the flow rather than the compressive portion. Because shocks such as $1 \rightarrow 2$ and $3 \rightarrow 4$ in Figure 9.8 occur in the expansive portion, only the shocks originating on the wing are expected to collide. In the present section, these shocks originate in the compressive portions of the flow, i.e., the region in the neighborhood of the stagnation points. Thus, collisions will occur between shocks on either side of the leading and trailing edges. We believe that such considerations can be useful in predicting and explaining the qualitative global features of many flows.

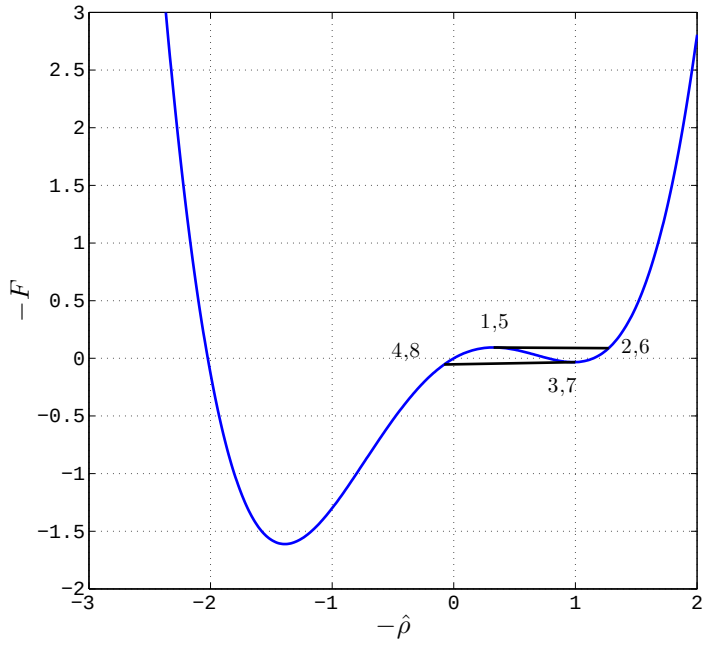

Figure 9.27: Rayleigh lines describing the strength and the type of shock waves present in the flow for the case with $\beta = 0.3$ and $K_1 = 0.6, K_2 = 0.1$, and $K_3 = -4$.

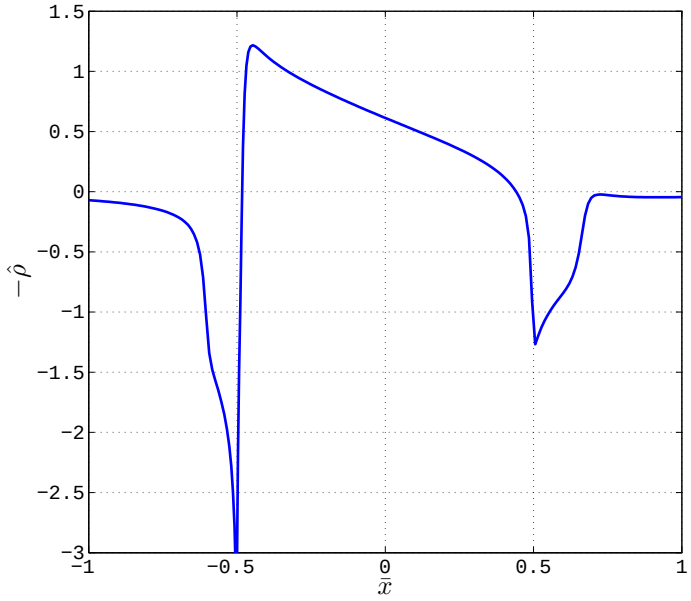

Figure 9.28: Density distribution of a subsonic free stream flow with $\beta = 0.3$ and $K_1 = 0.6, K_2 = 0.1$ and $K_3 = -4$.

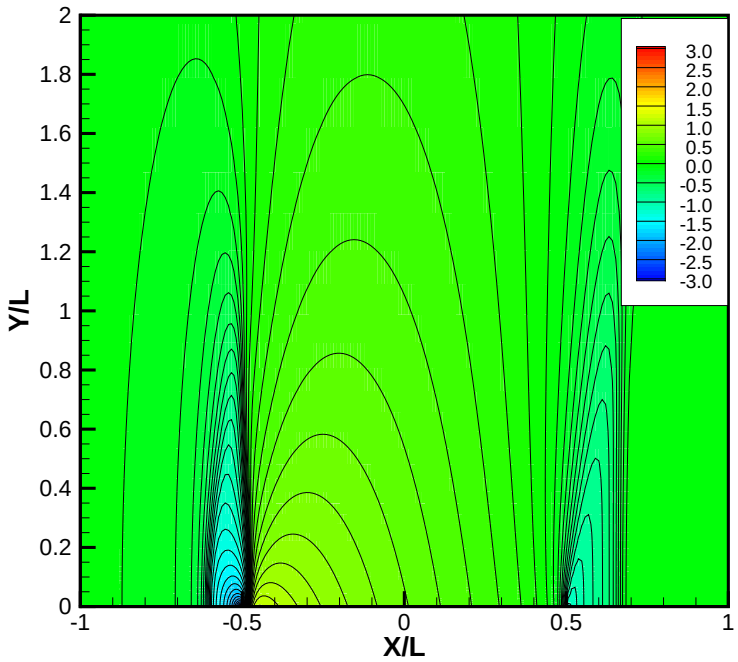

Figure 9.29: Contour plot of the density distribution of a subsonic free stream flow with $\beta = 0.3$ and $K_1 = 0.6, K_2 = 0.1$, and $K_3 = -4$. Contour steps of $\Delta\hat{\rho} = 0.1$

Next we increase the thickness of the wing and take $\beta = 0.5$. Figure 9.30 shows the Rayleigh lines that describe the behavior of the flow. The flow starts at the origin as always, and behaves in a similar manner as in the $\beta = 0.3$ case. The flow then keeps expanding to its minimum $\hat{\rho}$ value, at which point a normal shock develops from $5 \rightarrow 6$. As the flow continues toward the tail of the wing, it goes back to stagnation causing another normal shock on the wing from $7 \rightarrow 8$ (very close to the tail). The flow then has to expand back to free stream conditions, at which point it goes though another stern expansion shock from $9 \rightarrow 10$. The primary difference caused by the increase in the wing thickness is the formation of the normal compression shock $5 \rightarrow 6$. The density distribution on the wing and the contour plot from this case are provided in Figures 9.31 - 9.32. As in our discussion of Figure 9.26, we note that this new shock cannot collide with the other shocks on the wing and will decay to zero strength away from the wing.

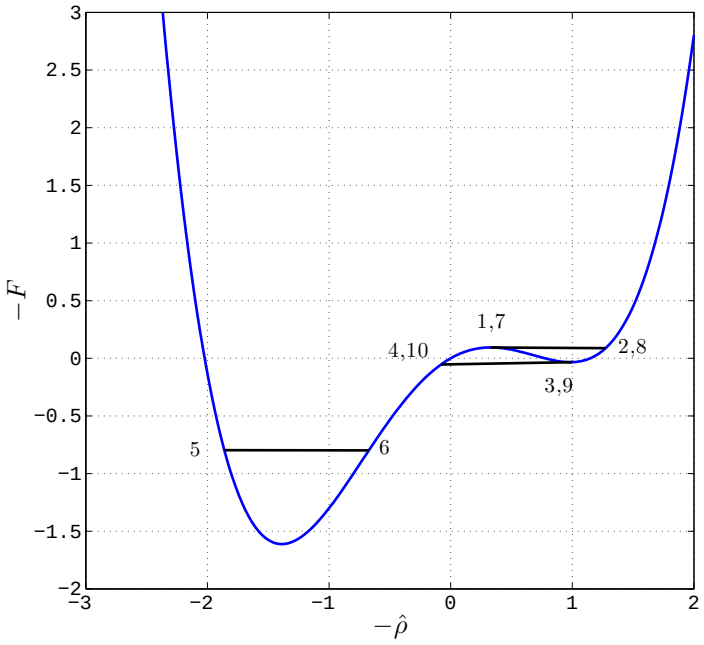

Figure 9.30: Rayleigh lines describing the strength and the type of shock waves present in the flow for the case with $\beta = 0.5$ and $K_1 = 0.6, K_2 = 0.1$, and $K_3 = -4$.

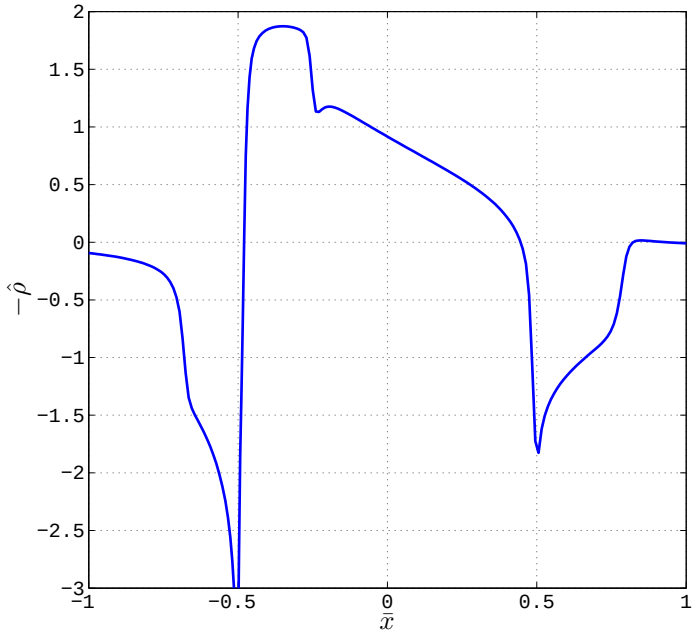

Figure 9.31: Density distribution of a subsonic free stream flow with $\beta = 0.5$ and $K_1 = 0.6, K_2 = 0.1$ and $K_3 = -4$.

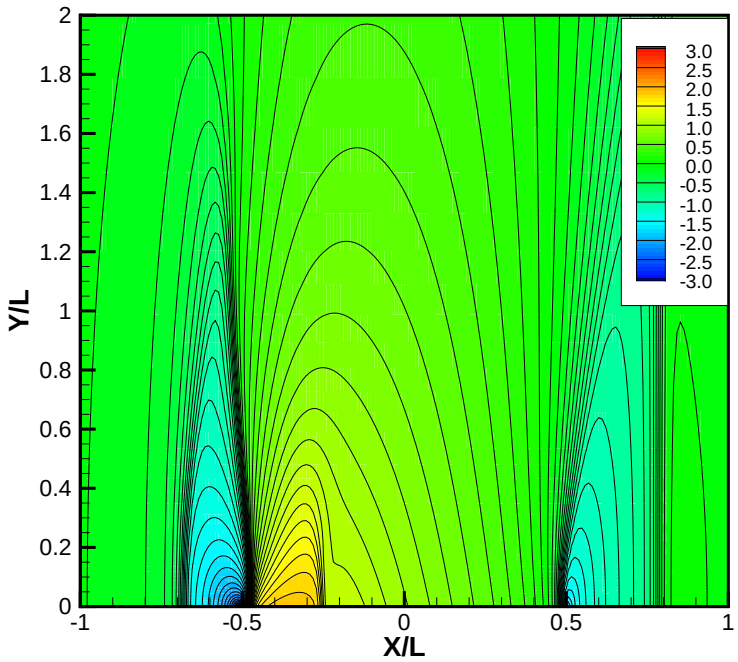

Figure 9.32: Contour plot of the density distribution of a subsonic free stream flow with $\beta = 0.5$ and $K_1 = 0.6, K_2 = 0.1$, and $K_3 = -4$. Contour steps of $\Delta\hat{\rho} = 0.1$

If we increase the thickness further by setting $\beta = 0.7$, the qualitative features of the flow does not change. The primary difference is the compression shock formed near $\bar{x} \approx 0.25$ is shifted toward the trailing edge in a manner similar to the classical behavior. The density distribution and contour plot for this case are provided in Figure 9.33-9.34.

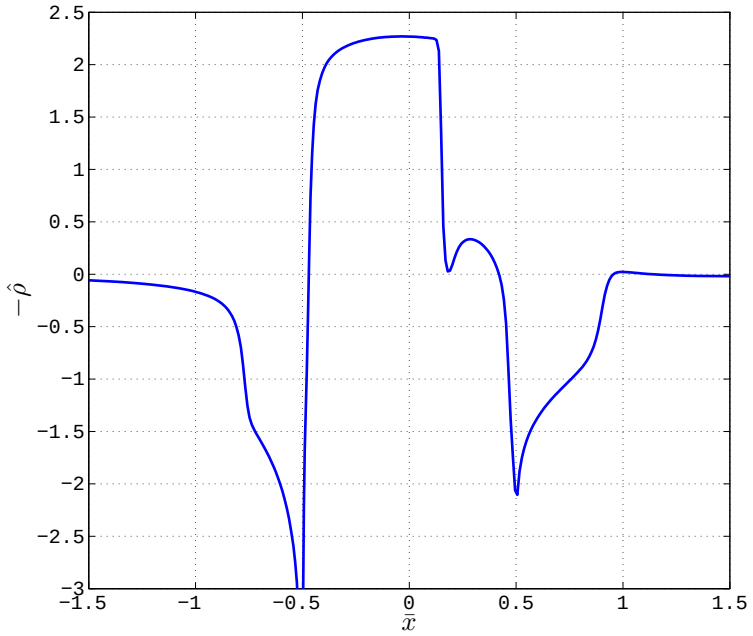

Figure 9.33: Density distribution of a subsonic free stream flow with $\beta = 0.7$ and $K_1 = 0.6, K_2 = 0.1$ and $K_3 = -4$.

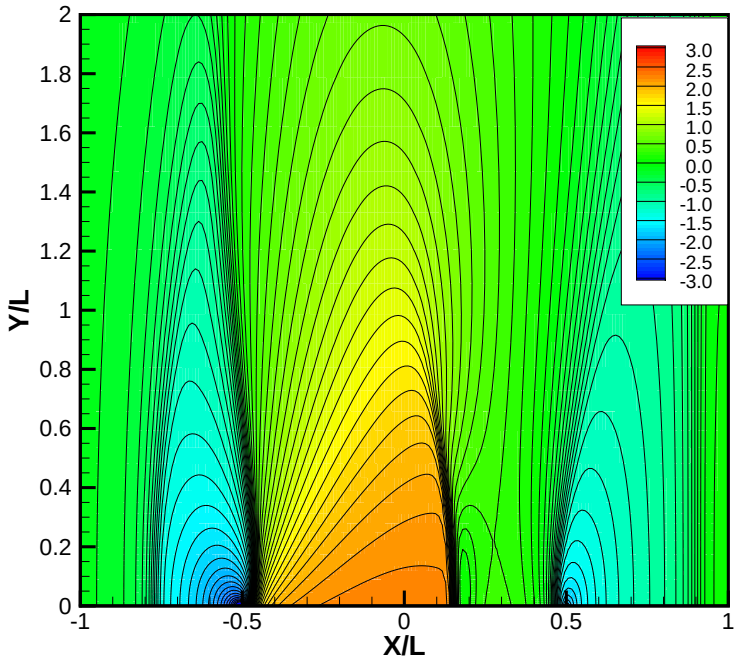

Figure 9.34: Contour plot of the density distribution of a subsonic free stream flow with $\beta = 0.7$ and $K_1 = 0.6, K_2 = 0.1$, and $K_3 = -4$. Contour steps of $\Delta\hat{\rho} = 0.1$

Increasing β to 0.9 has a similar effect as in the previous section involving split shocks. The two compression shocks on the wing from the $\beta = 0.7$ case combine to form a very strong normal shock as can be seen in Figure 9.35, which then splits in a similar manner discussed above. The computed flow has been plotted in Figures 9.36 - 9.37. The shock splitting is clearly seen in Figure 9.37. The bow shock and the stern shock remain of the same strength since the F curve is not manipulated.

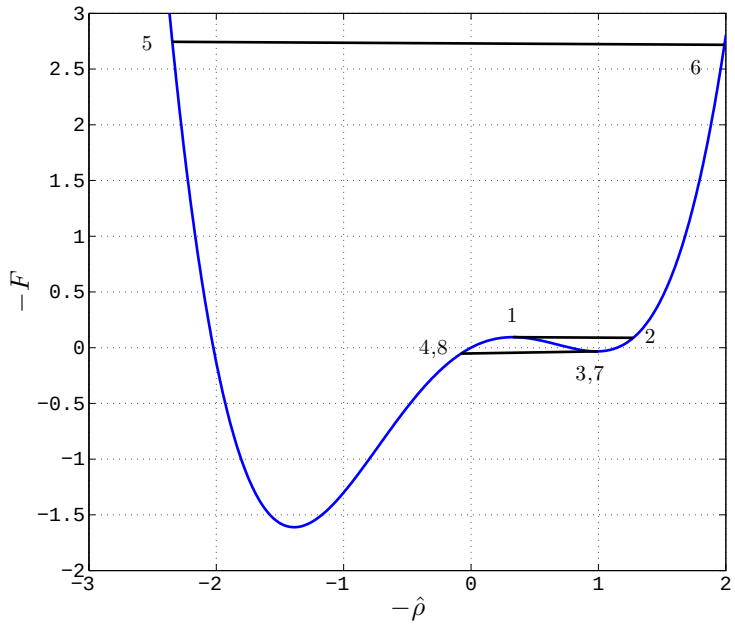

Figure 9.35: Rayleigh lines describing the strength and the type of shock waves present in the flow for the case with $\beta = 0.9$ and $K_1 = 0.6, K_2 = 0.1$, and $K_3 = -4$.

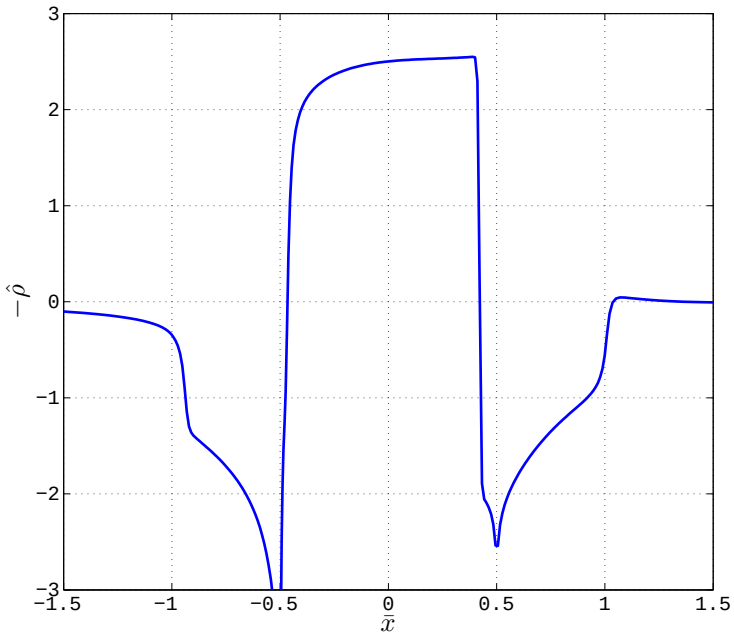

Figure 9.36: Density distribution of a subsonic free stream flow with $\beta = 0.9$ and $K_1 = 0.6, K_2 = 0.1$ and $K_3 = -4$.

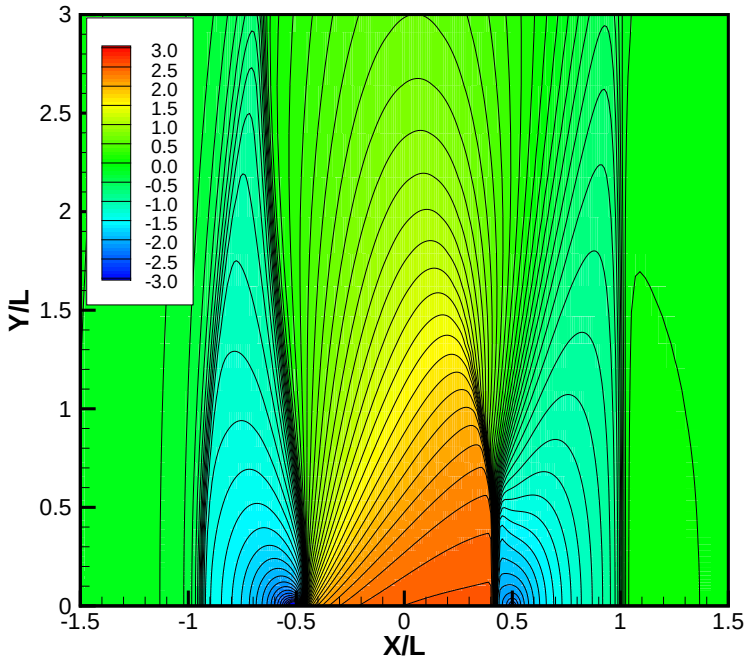

Figure 9.37: Contour plot of the density distribution of a subsonic free stream flow with $\beta = 0.9$ and $K_1 = 0.6, K_2 = 0.1$, and $K_3 = -4$. Contour steps of $\Delta\hat{\rho} = 0.1$

Lastly, setting $\beta = 1.2$, we observe three stern shocks. Figure 9.38 shows the progression of the flow and the computed flow details are provided in Figures 9.39 - 9.42. As can be seen in Figure 9.41, an oblique shock is now formed at the trailing edge; this shock is represented by the Rayleigh line $5 \rightarrow 6$ in Figure 9.38. For this case our numerical results generate a total of three normal stern shocks. The first two are compressive normal stern shocks represented by Rayleigh lines $7 \rightarrow 8$ and $9 \rightarrow 10$ in Figures 9.38. In Figure 9.39 these shocks are too close together to be easily resolved on the scale of the figure. However, the Mach number variations in Figure 9.40 clearly shows the re-acceleration to the sonic condition at 9. The separation of the shocks can also be seen in the contour detail shown in Figure 9.42. We regard this case as a transition case between that where the compressive stern shock is a single normal shock which takes the flow from the $-\hat{\rho} < 0$ portion of the F curve to the $-\hat{\rho} > 0$ portion, and the case where the Rayleigh line of the first stern shock corresponds to an $F < F_1$ resulting in two clearly separated compressive stern shocks. For this free stream thermodynamic state and free stream Mach number we were not able to get significant separation of the compressive stern shocks. Given the structure of the $-F$ vs. $-\hat{\rho}$ curve, we believe that such a transition can be realized and cases can be found with as many as three normal stern shocks, two of which are compressive and the third is expansive. However, the numerical verification may require slightly different K_i values.

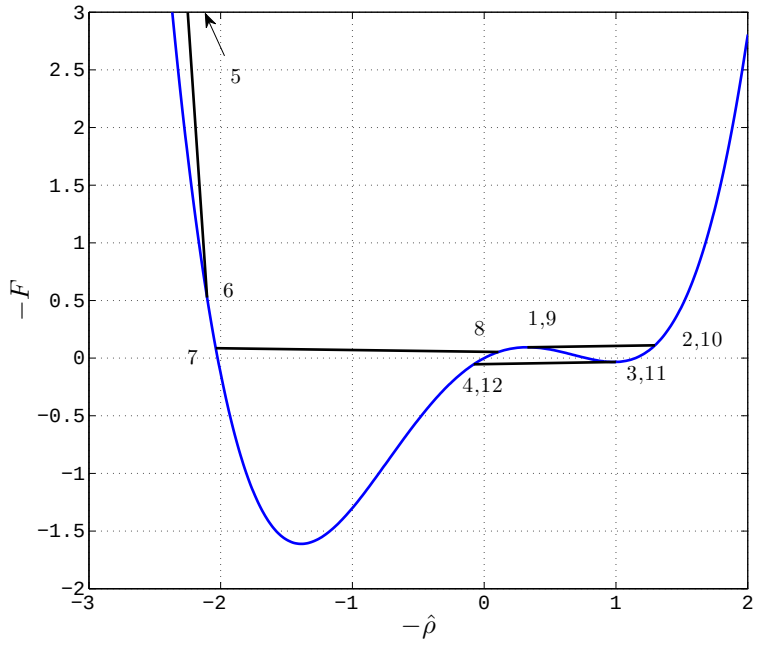

Figure 9.38: Rayleigh lines describing the strength and the type of shock waves present in the flow for the case with $\beta = 1.2$ and $K_1 = 0.6, K_2 = 0.1$, and $K_3 = -4$.

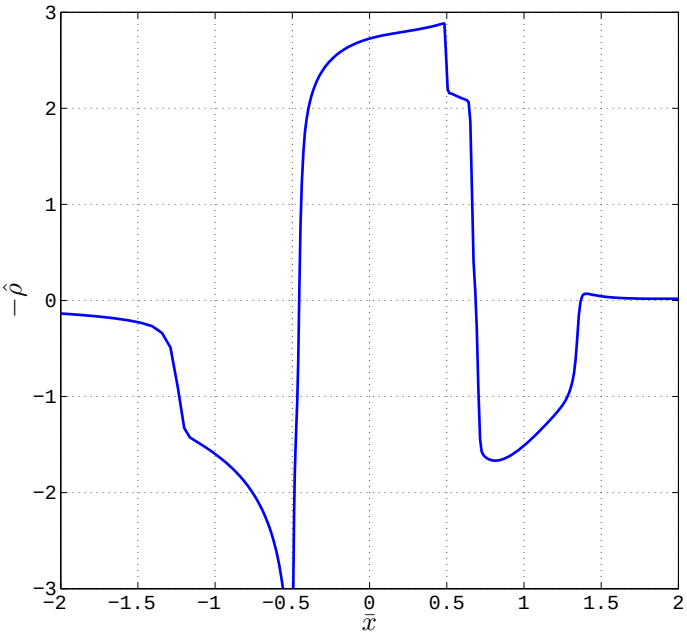

Figure 9.39: Density distribution of a subsonic free stream flow with $\beta = 1.2$ and $K_1 = 0.6, K_2 = 0.1$ and $K_3 = -4$.

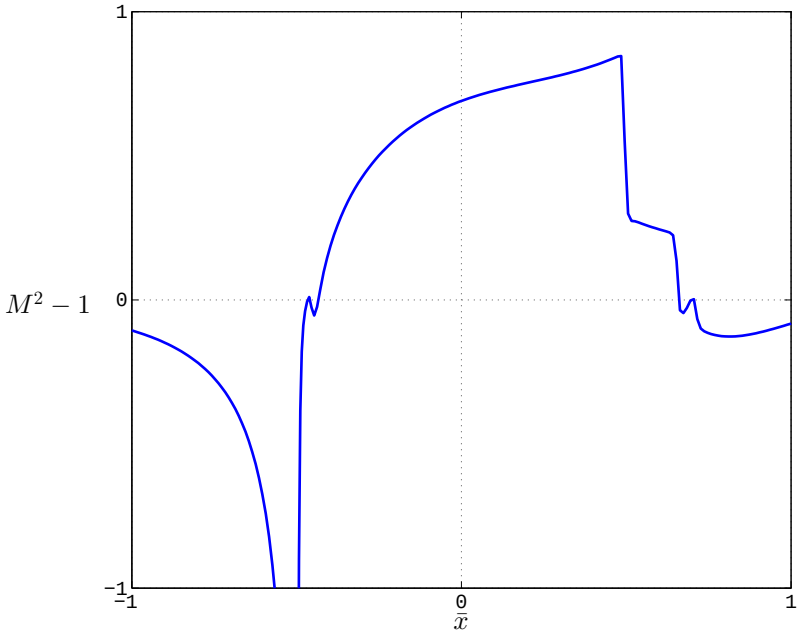

Figure 9.40: Mach number distribution of a subsonic free stream flow with $\beta = 1.2$ and $K_1 = 0.6, K_2 = 0.1$ and $K_3 = -4$.

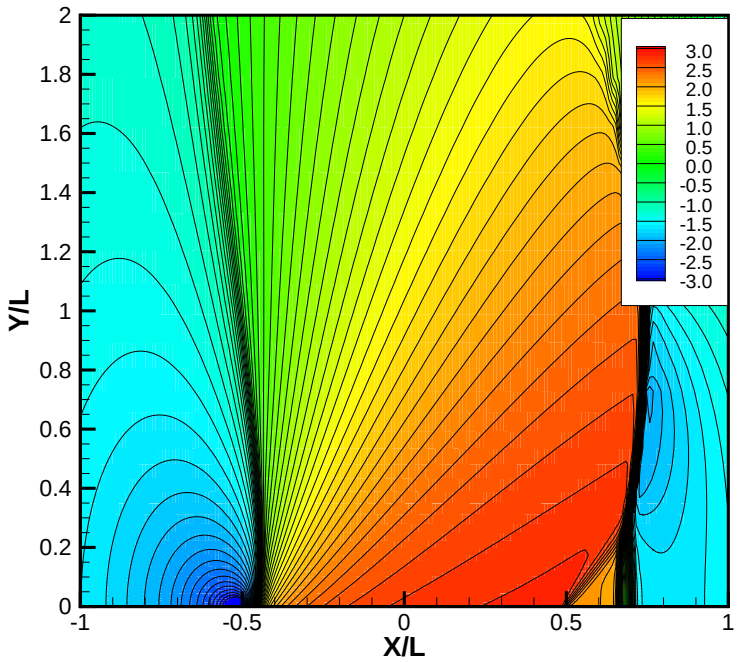

Figure 9.41: Contour plot of the density distribution of a subsonic free stream flow with $\beta = 1.2$ and $K_1 = 0.6, K_2 = 0.1$, and $K_3 = -4$. Contour steps of $\Delta\hat{\rho} = 0.1$

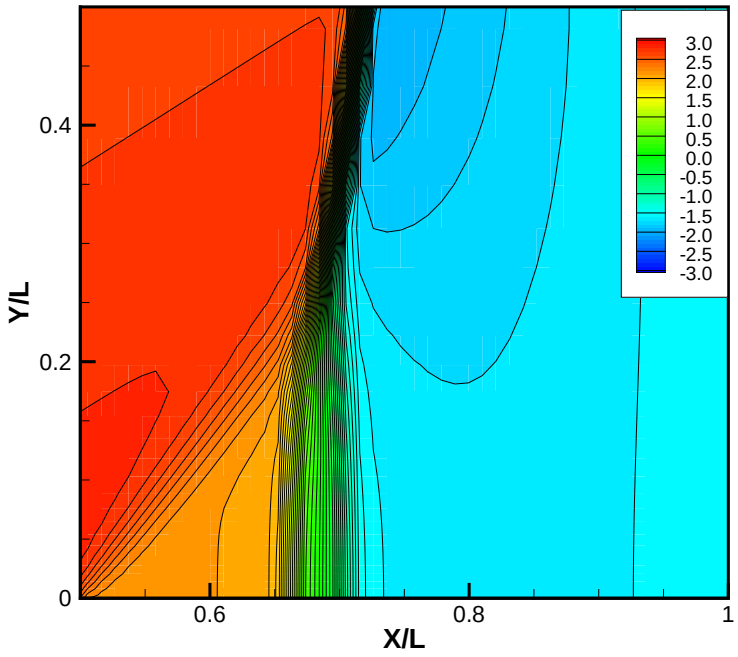

Figure 9.42: Two shocks close together with $\beta = 1.2$ and $K_1 = 0.6, K_2 = 0.1$, and $K_3 = -4$. Contour steps of $\Delta\hat{\rho} = 0.1$

9.0.3 Case 3: Supersonic Free Stream Flow With $K_2 < 0$ and $K_3 > 0$

The last case we consider is a flow over a NACA00XX wing with a supersonic free stream, positive $\tilde{\Gamma}_\infty > 0$, and $\hat{\Lambda}_\infty < 0$, meaning the free stream state is at a pressure below that of the low pressure zero of $\tilde{\Gamma}$. Figure 9.43 shows the F curve with two different values of K_1. We first consider the case where $K_1 = -1$ and $\beta = 1$. As the flow approaches stagnation, two compressive bow shocks must form from $1 \rightarrow 2$ and $3 \rightarrow 4$ as can be seen in Figures 9.44-9.46. The fact that two, rather than one large amplitude bow shock must occur follows from the basic existence conditions and the fact that the upstream state of the first shock must be at $\hat{\rho} = 0$. Another way to think about the generation of two bow shocks is to regard the first bow shock as re-initializing the flow to the state 2 in Figure 9.44. The reinitialized F curve is qualitatively the same as the $K_1 = 0.6$ F curve in Figure 9.23. The remainder of the flow then proceeds in roughly the same manner as that in previously discussed case. In particular, as the gas flows over the wing, the flow expands and goes through an expansion shock from $5 \rightarrow 6$. For the case considered here, the minimum $\hat{\rho}$ corresponds to point 7 in Figure 9.44. The flow then shocks through an oblique shock to point 8 in Figure 9.44. After the oblique shock, the flow goes back to free stream conditions.

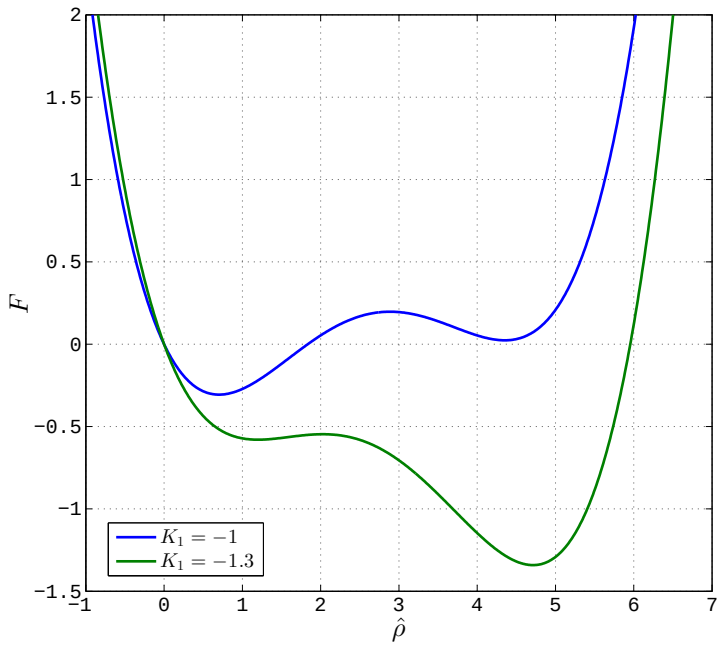

Figure 9.43: F curves for the third case with varying K_1 and $K_2 = -0.9, K_3 = 0.34$.

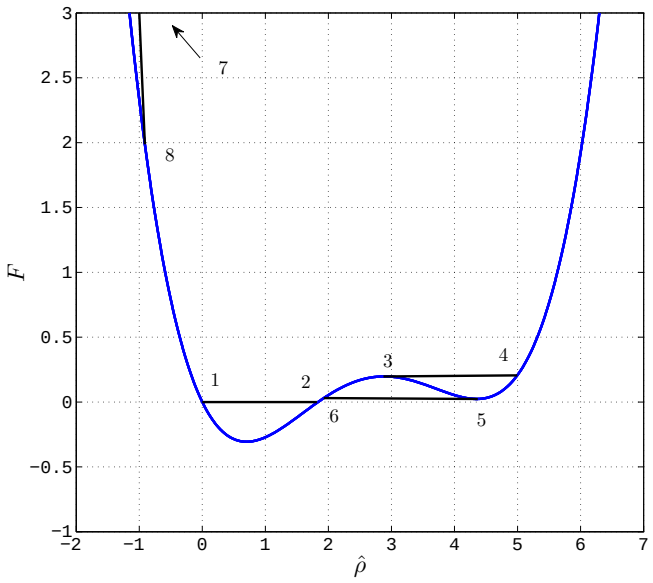

Figure 9.44: Rayleigh lines describing the strength and the type of shock waves present in the flow for the case with $\beta = 1$ and $K_1 = -1, K_2 = -0.9$, and $K_3 = 0.34$.

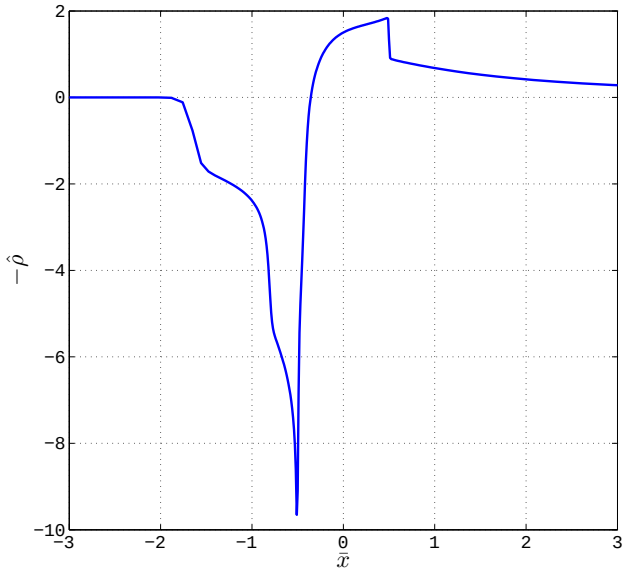

Figure 9.45: Density distribution of a supersonic free stream flow with $\beta = 1$ and $K_1 = -1, K_2 = -0.9$, and $K_3 = 0.34$.

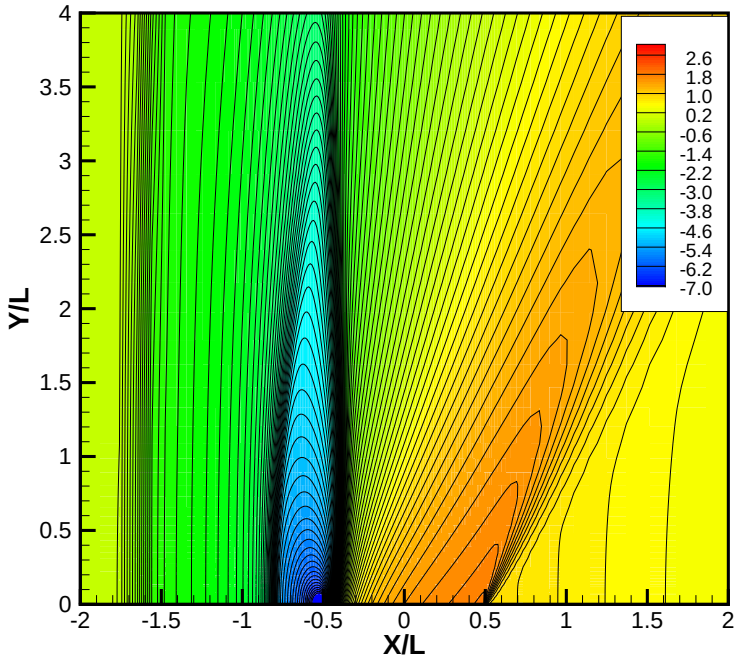

Figure 9.46: Contour plot of the density distribution of a supersonic free stream flow with $\beta = 1$ and $K_1 = -1, K_2 = -0.9$, and $K_3 = 0.34$. Contour steps of $\Delta\hat{\rho} = 0.1$

We now increase the free stream Mach number to the point where $K_1 = -1.3$, which lowers the local maximum of the F curve below the horizontal axis. The variation of F with labeled key points is provided in Figure 9.47 and the flow is depicted in Figures 9.48 - 9.49. This causes the two bow shocks from the $K_1 = 1$ case to merge, yielding a single compressive bow shock. As we move away from the wing this bow shock weakens. Because the upstream state must be point 1, the weakening is due to $\hat{\rho}_2$ decreasing until its Rayleigh line intersects the F curve, thus rendering the bow shock inadmissible. The bow shock then necessarily splits as discussed in Chapter 6. The split-shock is clearly seen in the contour plot Figure 9.49.

After leaving the stagnation point at the leading edge, the flow over the wing encounters the supersonic region between approximately $\hat{\rho} = 1$ to $\hat{\rho} = 2$ and generates the normal sonic expansion shock seen in Figures 9.48 - 9.49. At the minimum value of $\hat{\rho}$, the flow is compressed back to the free stream value through an oblique shock at the trailing edge.

If we examine the flow away from the wing, the expansion shock may or may not collide with the second (downstream) compression shock from the shock splitting. Whether it does or not will depend on the detailed evolution of the expansion shock. However, analysis of the F curve in Figure 9.47 shows that the expansion shock necessarily collides with the leading bow shock. The result of this collision is a single compressive bow shock which continues to infinity as seen in Figure 9.50.

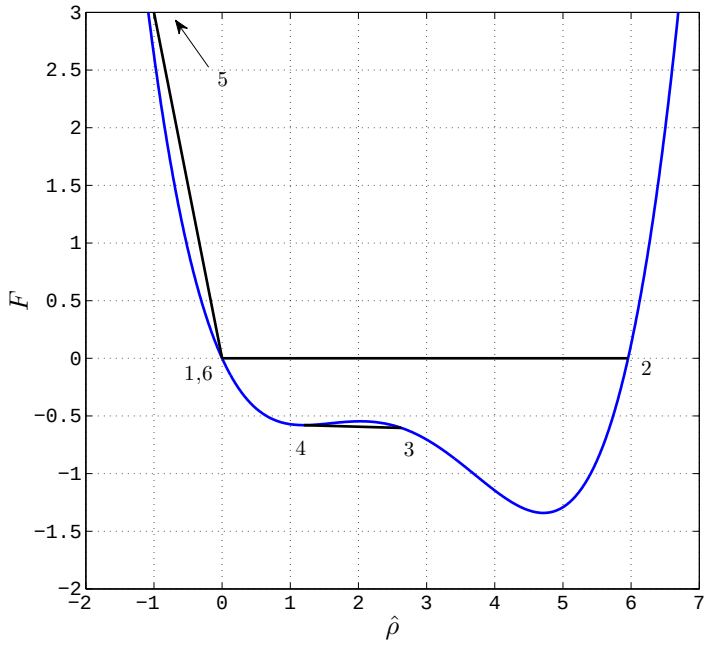

Figure 9.47: Rayleigh lines describing the strength and the type of shock waves present in the flow for the case with $\beta = 1$ and $K_1 = -1.3, K_2 = -0.9$, and $K_3 = 0.34$.

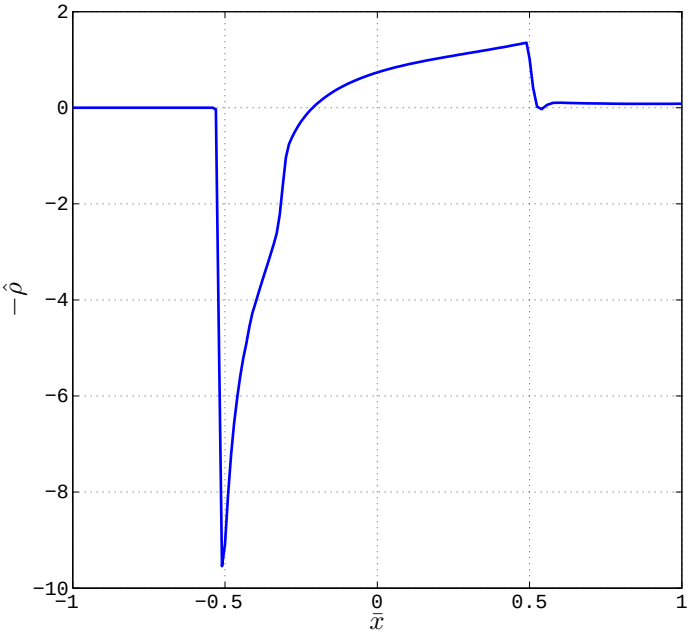

Figure 9.48: Density distribution of a supersonic free stream flow with $\beta = 1$ and $K_1 = -1.3, K_2 = -0.9$, and $K_3 = 0.34$.

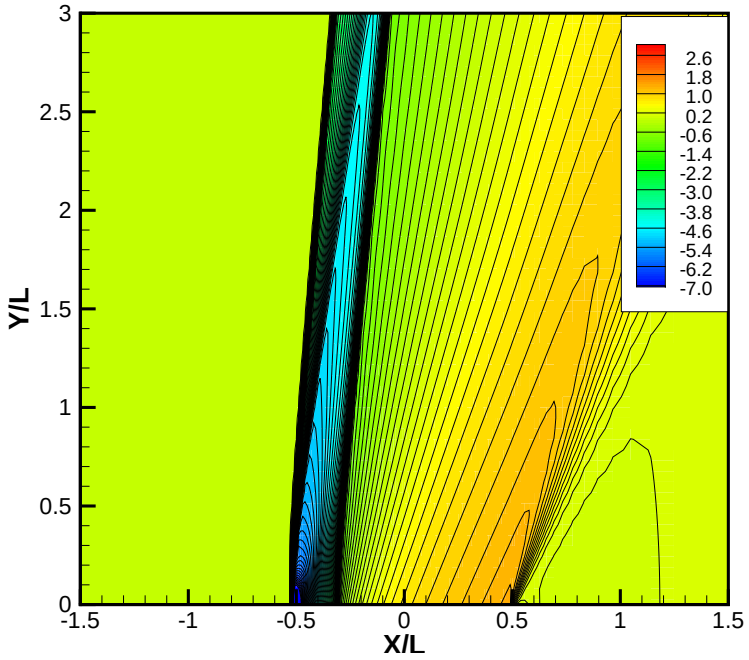

Figure 9.49: Contour plot of the density distribution of a supersonic free stream flow with $\beta = 1$ and $K_1 = -1.3, K_2 = -0.9$, and $K_3 = 0.34$.. Contour steps of $\Delta\hat{\rho} = 0.1$

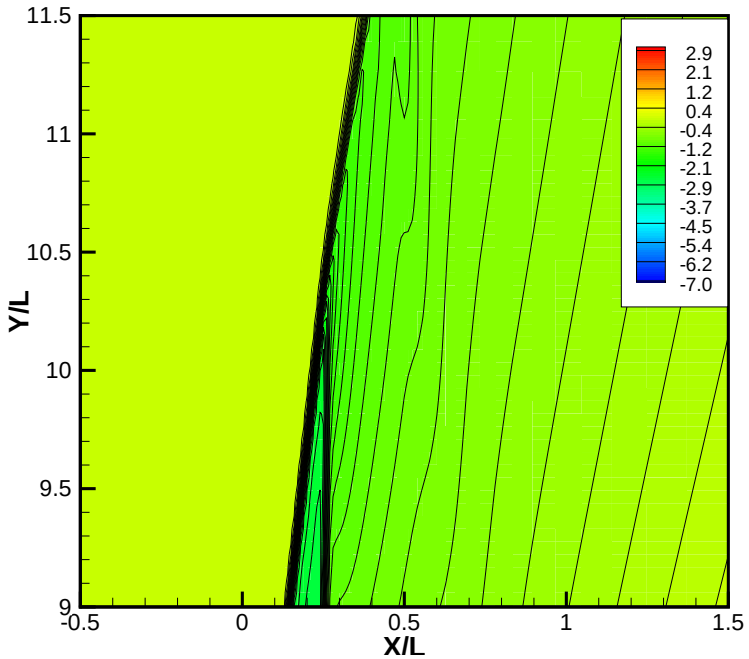

Figure 9.50: Contour plot of the density distribution at the collision of the leading bow shock with the expansion shock of a supersonic free stream flow with $\beta = 1$ and $K_1 = -1.3, K_2 = -0.9$, and $K_3 = 0.34$. Contour steps of $\Delta\hat{\rho} = 0.1$

Chapter 10

Summary

We have derived a transonic small disturbance equation capable of describing the primary qualitative behavior of BZT fluids in steady, two-dimensional, transonic flows over thin single wings and turbine blades. In order to capture the parabolic character of the fundamental derivative, it was necessary to include two thermodynamic parameters Λ_∞ and Ξ_∞ as defined in (5.13). As a result, we find that transonic flows of BZT fluids are governed by four similarity parameters: K_1, K_2, K_3, and the sign of $\tilde{\Gamma}_\infty$. This is three more than in the case where the fluid is a perfect gas or in which the fundamental derivative is always positive, and one more similarity parameter than required in the theory of [2].

The most significant difference between the theory presented here and that found in the perfect gas theory is that the flux function (5.15) is quartic and not quadratic in the pressure or velocity disturbance. As a result, the flux function is non-convex, which, once the existence conditions are considered, gives rise to the complex gasdynamic phenomena observed in the present study.

Shock jump conditions and the basic existence conditions have been stated in Chapter 6. Because of the complexity of the physical phenomena, it is fortunate that the shock existence conditions as well as most of the flow can be described entirely in terms of the shape of the F vs. $\hat{\rho}$ curve and the straight lines, called Rayleigh lines, connecting the upstream and downstream states on the F curve. These geometric interpretations are similar to those used in the general theory, see, e.g., [12], but our restriction to thin wings and small disturbances ensures that the shock adiabat, isentropes, and F vs. $\hat{\rho}$ curve all represent the same process which simplifies the analysis considerably.

The derived TSDE has been solved numerically using successive line relaxation with a variable mesh following [1] - [2] for both supersonic and subsonic free streams and a slightly modified NACA 00XX series symmetric airfoil. The analysis of the F curves has been used to predict and explain the phenomena observed in our numerical computations.

While many of the phenomena revealed by our computations have been seen elsewhere in

either published or unpublished studies, we believe the analysis of the F curves can provide a more direct and reliable tool for predicting and understanding the behavior. Previous methods, which were primarily based on the variation of the Mach number on an isentrope, could not straightforwardly take advantage of the basic existence conditions. Phenomena predicted and observed here which were not described elsewhere are the splitting of normal and oblique shocks and the transition to merged shocks, the conditions under which normal expansion shocks are possible, and the prediction and observation of multiple stern shocks.

Bibliography

[1] Murman, E.M. and Cole J.D. 1971, Calculation of Plane Steady Transonic Flow. AIAA J. 9, 114-121.

[2] M.S. Cramer and G.M. Tarkenton,"Transonic Flow of Bethe-Zel'dovich-Thompson fluids", Journal of Fluid Mechanics, Volume 240, 10 December 1992, pp. 197-228.

[3] Cramer, M.S Tarkenton, L.M., and Tarkenton, G.M., "Critical Mach Number Estimates For Dense Gases", Physics of Fluids, Volume 4, 1992, pp. 1840-1847.

[4] Michael D. Gibbons and John T. Batina, "Supersonic Far-Field Boundary Conditions for Transonic Small-Disturbance Theory", Journal of Aircraft,Volume 27, No. 9.

[5] Anderson, J.D., "Modern Compressible Flow with Historical Perspective",McGraw-Hill, NY, 1982.

[6] Fletcher, C.A.J., "Computational Techniques for Fluid Dynamics 2",Springer-verlog, Berlin Heidelberg, NY, 1988

[7] Andreson, J.D., "A History of Aerodynamics, Cambridge University Press", Cambridge, 1997.

[8] Abbot, R.H. and Doenhoff, A.E, "Theory of Wing Sections", Dover 1959.

[9] Thompson, P.A., "A Fundamental Derivative In Gasdynamics", Physics of Fluids, Vol. 14, 1971, pp. 1843-1849.

[10] Thompson, P.A., "Compressible-Fluid Dynamics", McGraw-Hill, NY, 1972.

[11] Lambrakis, K and Thompson, P.A., "Existence of real fluids with a negative fundamental derivative Γ", Physics of Fluids, Vol. 15, 1972, pp. 933-935.

[12] Thompson, P.A. and Lambrakis, K., "Negative shock waves", Journal of Fluid Mechanics, Vol. 60, 1973, pp. 187-208.

[13] Cramer, M.S., and Park, S. 1999, "On The Suppression of Separation of Shock-induced Separation In Bethe-Zel'dovich-Thompson Fluids," Journal of Fluid Mechanics, Vol. 393, 1999, pp. 1-21.

[14] Morren, S.H., "Transonic Aerodynamics of Dense Gases", M.S. Thesis, Virginia Polytechnic Institute and State University, Blacksburg, VA, 1990.

[15] Morren, S.H., "Transonic Aerodynamics of Dense Gases", NASA TM 103732, 1991.

[16] Morrison, M.J., "Accurate Equation of State in Transonic Flows of Arbitrary Gases", Senior Project Report, Virginia Polytechnic Institute and State University, Blacksburg, VA, 1997.

[17] Cramer, M.S. and Morrison, M.J., "Lifting Transonic Flows of Pressurized Gases", AIAA Paper AIAA-98-2689, 1998.

[18] Trappe, S., "Realgaseinflüsse auf Profilum Strömungen:,Studienarbeit, Institut für Strömungs lehre und Strömungsmaschinen, Universität Karlsruhe (TH), Karlsruhe, Germany, 1994.

[19] Cinnella, P. and Congedo, P.M., "Aerodynamics Performance of Transonic Bethe-Zel'dovich-Thompson Flows Past an Airfoil", AIAA Journal, Vol. 43, 2005, pp.370-378.

[20] Cinnella, P. and Congedo, P.M., "Inviscid and Viscous Aerodynamics of Dense Gases", Journal of Fluid Mechanics, Vol. 580, 2007, pp. 179-217.

[21] Cinnella, P., "Transonic Flows of Dense Gases over finite wings", Physics of Fluids, DOI: 10.1063/1.2907212, 2008.

[22] Zierep, J., "New Results for the Normal Shock in Inviscid Flow at a Curved Surface", Journal of Applied Mathematics and Mechanics ,DOI: 10.1002/zamm.200310051